Fluid-Thermal-Structural Interactions Induced by an Asymmetric Shock-Wave/Boundary-Layer Interaction in a Mach-6 Compression Corner

Travis A. Duchene, Antonio Giovanni Schöneich, and Stuart J. Laurence
University of Maryland, College Park, MD 20742, USA

Brett F. Bathel, Joshua M. Weisberger, and Gregory M. Buck
NASA Langley Research Center, Hampton, VA 23666, USA

Daniel J. Bodony
University of Illinois Urbana-Champaign, Urbana, IL 61801, USA

An experimental study is conducted of the fluid-thermal-structural interaction of a clamped compliant panel exposed to a three dimensional shock-wave/boundary-layer interaction (SWBLI) induced by a Mach-6 compression ramp with a spanwise nonuniform incoming boundary layer. The nonuniform boundary layer was produced by placing trips on one side of the upstream flat plate, resulting in largely turbulent flow on the tripped side and transitional flow on the untripped side. Measurements of the flowfield confirmed that the tripped boundary layer contained elevated levels of unsteadiness, and the SWBLI was observed to vary from attached to fully separated as the ramp angle was increased from $10°$ to $38°$; the separation region on the tripped side of the panel was noticeably smaller, showing the elevated turbulence levels of the tripped-side flow to remain relatively localized rather than diffusing across the whole model. Full-field, time-resolved panel deformations were measured using high-speed photogrammetry and the vibrational response at each compression angle was characterized. Although the measured modes conformed largely to those from classical clamped-plate theory, some skewing of the mode shapes was observed. IR thermography highlighted regions of the compliant region where elevated temperatures were likely to promote thermal softening effects to the transient panel response. The quasi-static deformation and stress field was used to characterize the internal stress factor of each mode and showed a meaningful relationship between transient panel response and stress contained within each mode: modes with antinodes lying in high-stress areas of the plate tended to exhibit increases in vibrational frequency and decreases in vibrational power, whereas the opposite was true for modes with antinodes in low-stress areas.

I. Introduction

Reusable hypersonic flight is accompanied by complex aero-thermal loading, which remains difficult to predict; in particular, shock-wave / boundary-layer interactions (SWBLIs) further complicate the flow environment and thus challenge predictions of vehicle performance. Design requirements for reusable hypersonic vehicles tend to favor long, slender configurations and require lightweight and durable structural components [1], which can be susceptible to, and potentially couple with, the aero-thermal loading environment. Shortcomings in predicting mechanical and thermal loads, and the resulting structural responses of the coupled fluid-thermal-structural interaction (FTSI), have led to over-design of current thermal protection systems and overly conservative structural design margins [2]. Specifically, assessing the effects of localized heating and pressure loading caused by SWBLIs on vehicle panels remains a paramount concern as these SWBLIs can lead to boundary-layer separation with a corresponding low-frequency unsteady motion capable of coupling with compliant surface structures [3–6]. In regard to the FTSI problem, the elevated pressure fluctuations near shear-layer reattachment for separated SWBLIs are expected to bring about complex and severe interactions [7]. Furthermore, such surface vibrations, being influenced by the surface thermomechanical distribution, can in turn influence the fluid field, leading to a multi-directional coupling between fluid and structure [8, 9]. Also, the intense aero-thermal loading on thin compliant regions has been found to induce significant static deflections, on the order of the panel thickness and greater, which greatly alter the vibrational characteristics of such structural elements

[10].

Earlier developments in the modeling of high-speed fluid-structural interactions (FSIs) and FTSIs made use of simple aerodynamic models suitable for single panels [11–14], wings [15, 16], and conceptual vehicles [17, 18]. More recent work has shown that structural vibrations can couple with and alter the downstream flowfield, unsteady shock dynamics, and flow separation behavior [6, 10, 19–21]. Further, investigations of the two-way aerothermoelastic coupling have demonstrated the underlying importance of the nonlinear temperature-dependent structural response [14, 22] and the dependency of the panel oscillation frequency on the back pressure and temperature differentials between connecting structural elements of differing thicknesses [23]. There is still much to be desired concerning our understanding of hypersonic FTSIs, however, particularly under SWBLI excitation, and a need for validation-quality experimental data, including measurements of the relevant fluid features, surface aero-thermal loads, and flexible panel response.

The two-dimensional compression-ramp-induced SWBLI is a canonical geometry that is well described at low supersonic Mach numbers [24–26]; however, the same configuration has received less attention for hypersonic flight conditions at which the effects of heating and low-frequency flow unsteadiness are expected to be amplified. From an FTSI perspective, Whalen et al. [7, 27] found severe pressure fluctuations near shear-layer reattachment for separated SWBLIs at Mach 6 on a compliant region embedded in the ramp; in these cases, there was a higher than expected degree of static deformation and vibrational frequency shifting, likely caused by the thermal stresses introduced by the temperature differential between the compliant panel and the support. In measurements on a similar configuration with a variable back pressure, it was found that an increased pressure differential across the compliant panel introduced additional stresses and reduced vibrational response, which resulted in a reduction of pressure fluctuations upstream of the corner for nominally transitional incoming boundary layers [28]. A downshifting in structural natural frequencies was attributed to increased temperature differentials, but the unavailability of flow visualization meant that it was not possible to assess how the potential shifting of the flow re-attachment point on the compliant panel contributed to changes in the mechanical response. At Mach 10, Duchene et al. [10] identified significant static deflection occurring on a compliant region, which heavily altered the vibrational characteristics; noticeable changes were found in both the transient vibrational behavior as well as the spatial distribution of node/antinode locations. In all of these prior studies, the underlying SWBLI flowfield was nominally two-dimensional, with a spanwise uniform incoming boundary layer. On a real vehicle, however, nonuniform boundary-layer transition could result in an asymmetric, three-dimensional flow configuration, even if the generating geometry is two-dimensional. In such cases, we might expect nonuniform temperature distributions and mechanical loading environments to develop, further complicating the panel response.

Therefore, in this work, we employ experiments to assess the response of a fully-clamped compliant metallic panel to a compression-ramp-induced Mach 6 SWBLI with a half-tripped incoming boundary layer. This paper is organized as follows. Section II describes the test facility, model, and diagnostic techniques for the experiments performed. In Sections III.A through III.C, we characterize the state of the incoming boundary layer, the SWBLI flowfield for each ramp angle, and the thermal environment of the compliant region. Sections III.D through III.F present findings on the non-linear structural response of the compliant panel to the SWBLI aero-thermal loading. Conclusions are then drawn in Section IV.

II. Experimental Setup

A. Facility

All experiments were conducted in the NASA Langley 20-Inch Mach 6 Hypersonic Wind Tunnel. This is a conventional blow-down wind tunnel facility that uses heated dry air as the test gas. As a blow-down facility, steady flow times can exceed 15 minutes, though due to camera memory limitations, run times for the present campaign were limited to approximately 10 seconds on condition. Nominal reservoir conditions give stagnation temperatures of $420 - 520$ K and stagnation pressures of $0.21 - 3.3$ MPa, corresponding to unit Reynolds numbers of $1.6 - 23.6 \times 10^6\ 1/m$. The present research examined SWBLIs on a flat-plate/ramp at unit Reynolds number of $6.6 \times 10^6\ 1/m$, which produced a transitional incoming boundary layer under untripped conditions. Table 1 provides the freestream flow parameters for the present experiments.

Before each run, the test section, nozzle, and settling chamber were pulled down to low pressure by opening a valve to an adjoining vacuum sphere. The model was subsequently injected into the test section in order to collect flow-off data. The model was then retracted into the injector box, at which point a valve upstream of the settling chamber started the tunnel. Once the desired freestream conditions were reached, the model was again injected into the test section, signaling t_0 of the test time. The test section has three windows for optical access (one on top and two on the sides) and

Table 1 Run Conditions

M_∞	Re_∞	p_∞	ρ_∞	T_∞	v_∞	δ_0
5.96	$6.6 \times 10^6\ 1/m$	0.57 kPa	0.032 kg/m^3	62.7 K	946 m/s	4.6 mm

a cross-section of 520 x 508 mm. For the present experiments, the top, front window was fitted with a special Zinc Selenide (ZnSe) antireflective-coated window, enabling infrared (IR) thermography measurements [29].

B. Model

The test article was a steel flat plate with a compression corner; a CAD rendering of the model is shown in the left image of Figure 1. The base of the model consisted of a 280 mm wide by 711 mm long flat plate with a sharp leading edge and a 102 mm wide channel along the centerline for inserts. In the present experiments, this insert was instrumented with Kulite® and PCB® pressure transducers; the spacing of these sensors is shown in the right image of Figure 1. A 15-5 PH/H1025 (AMS 5659) stainless steel ramp was placed 356 mm downstream of the leading edge to generate the compression corner. The ramp was 203 mm wide by 102 mm long, with a thickness of 7.62 mm. A compliant configuration was examined in which a rectangular cavity measuring 76.2 mm by 88.9 mm was machined out of the rear of the ramp, resulting in a 0.5 mm thick, fully clamped compliant panel embedded in the ramp surface. The ramp side edges were machined to a sharp point such that, when the ramp assembly was inserted into the flat plate, the leading edge of the ramp was flush with the surface of the plate. The upstream edge of the compliant panel was collocated with the corner of the compression ramp. The ramp was placed on interchangeable angled brackets to produce nominal ramp angles of 10°, 20°, 30°, 34°, and 38°, spanning flow conditions from attached to fully separated SWBLIs (as shall be discussed shortly). To generate the spanwise nonuniform incoming boundary layer at the SWBLI, a half-spanwise array of 7 boundary-layer trips were placed 87.4 mm downstream of the leading edge to promote the development of a half-turbulent-half-transitional boundary-layer near the ramp region. Each tripping element had a square diamond shape with a side length of 2.16 mm and a height of 3.05 mm; the center-to-center spacing was 6.6 mm, with the corner of the diamond oriented into the flow, and the inner-most tripping element was located 12.8 mm away from the model centerline. Select results are presented for the same plate/ramp configuration without the half-span flow trips to compare the effects of the asymmetric SWBLI.

A plenum box was used to create a pressure-controlled environment on the back-side of the panel, in principle allowing changes to the structural dynamics caused by varying a pressure differential across the compliant panel to be studied. The cavity generated by the plenum box and ramp measured 15.7 mm deep and was controlled by a 15 psia (103 kPa) pressure calibration unit (for a representative image of this setup refer, to refs. [10, 28]). In the present experiments, the back pressure for each ramp angle was chosen to match the inviscid static, post-oblique shock pressures,

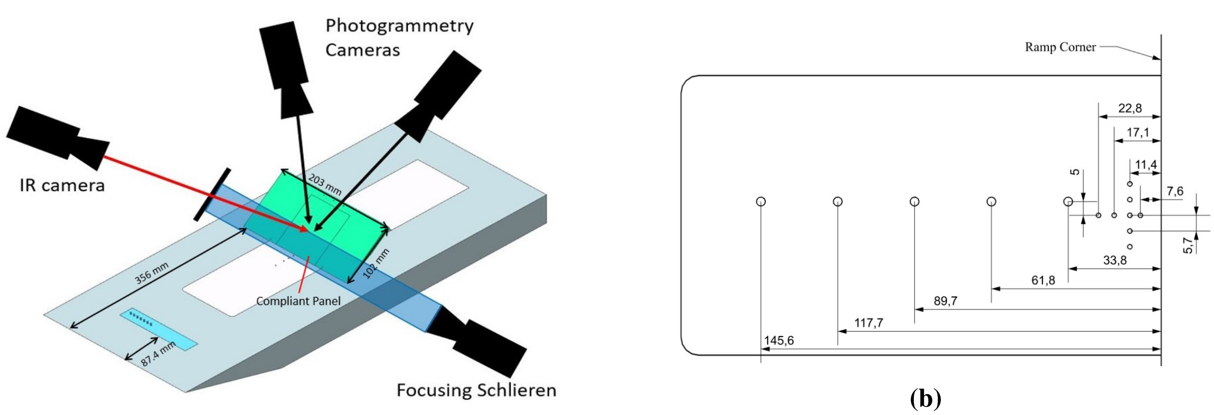

(a)

(b)

Fig. 1 (a) Schematic of flat-plate/ramp model with viewing paths for each diagnostic technique and (b) layout of pressure sensors along the model centerline (dimensions in mm).

p_2, giving a nominal pressure differential of $\Delta p = 0$ kPa.

The flat plate was instrumented with seven flush-mounted fast-response, piezoresistive Kulite pressure transducers and five 132B38 high-frequency PCB transducers. The placements for each of these pressure sensors on the upstream portion of the plate are shown in the right image of Figure 1, with the larger circles denoting PCB locations. Note that we define the streamwise distance from the corner, x_c, as negative along the flat plate upstream of the corner and positive parallel to the downstream ramp surface. The plenum box was instrumented with two XCE-062 Kulite pressure transducers to monitor the static pressure fluctuations inside the cavity behind the panel. All Kulite signals were collected by three Dewetron TRION-2402-dSTG universal input modules at 200 kHz. The PCB transducers were routed through two PCB Model 482C signal conditioners and their signals were collected by two Dewetron TRION-1620-ACC input modules at 2 MHz with an antialiasing filter of 500 kHz. All Kulite sensors were equipped with protective B-screens (i.e., circular arrangement of eight 0.15 mm holes), with a flat response for frequencies $\lesssim$ 16 kHz [30].

Pre-campaign modal testing of the compliant panel was conducted using an impulse hammer and a Polytec PSV-300 scanning vibrometer (with a sampling frequency of 100 kHz) to characterize panel natural frequencies. Four interrogation locations were chosen for excitation that lay away from nodes of the six lowest-frequency modes; data was collected for a zero pressure gradient across the panel. Table 2 shows the measured natural frequencies of these six modes together with theoretical results from Freydin and Dowell [31]. The maximum uncertainty in $f_{vibrometer}$ with a 95% confidence level was found to be 1.15×10^{-4} kHz. The theoretical predictions are generally higher than the measured values, though this trend is reversed for the (1,3) and (3,1) modes. This is thought to be a result of non-ideal structural boundary conditions, in which panel edges are not perfectly clamped but are more akin to a clamped-pinned boundary condition.

Table 2 Nominal Wind-Off Panel Modes

Mode Shape	(1,1)	(2,1)	(1,2)	(2,2)	(3,1)	(1,3)
$f_{theoretical}$ [kHz]	0.67	1.19	1.43	1.94	1.96	2.07
$f_{vibrometer}$ [kHz]	0.51	1.09	1.16	1.75	1.99	2.35

C. Focusing Schlieren

Given the expected spanwise variation of the SWBLI, the path-integrated nature of conventional schlieren systems would make interpretation of the visualized flow field difficult. Instead, a self-aligned focusing schlieren (SAFS) system was used to isolate the schlieren response to a narrow depth-of-field, effectively reducing the influence of density gradients outside the plane of interest at the center of the model [32–34]. In the present implementation, a laser light source (Cavitar Cavilux HF) was loosely collimated and diffused through a condenser/diffuser lens, before passing through a linear polarizer and reflecting onto the main system optical axis by a polarizing beam splitter cube. The linear vertically polarized light back-illuminated a Ronchi ruling (Data Optics), then was projected and focused onto a retroreflective background (3M Scotchlite 7610) on the opposite side of the tunnel by a field lens (Nikon, 300 mm focal length). Between the Ronchi ruling and field lens, the light passed through a polarizing Rochon prism (United Crystals, glass/quartz, 7.5 arcmin splitting), and on the outgoing path, the linear vertically polarized light remained unrefracted. Just prior to the retroreflective background, a thin piece of quarter-wave film was oriented such that it converted the linear vertically polarized light to right-circularly polarized light. Upon retro-reflection, the handedness of the light was converted to left-circularly polarized, and upon return passage through the quarter-wave film, to linear horizontally polarized light. The field lens formed an image of the returning light back onto the Ronchi ruling, where the incoming light was refracted slightly by the Rochon prism due to its changed polarization state, providing an adjustment of the sensitivity of the system akin to the knife-edge cutoff in a conventional schlieren system. The light then passed through the polarizing beam splitter, through another linear polarizer to increase image contrast, and an image of the density object was formed at the camera sensor plane (Photron SA-Z) through the use of a relay lens (Niko AF Nikkor, 50 mm, 1:1.4D). The sensitivity of the SAFS system would be adjusted by focusing of the Ronchi ruling on the retroreflective background, and by adjusting the cutoff through the positioning of the Rochon prism relative to the Ronchi ruling. The plane-of-focus of the images was adjusted through the camera and relay lens position and focus. To provide sensitivity to both the horizontal and vertical density gradients in the flow simultaneously, the Ronchi ruling was rotated to 45 degrees relative to the freestream flow direction. Various Ronchi ruling line spacings were used throughout testing depending on the required sensitivity.

D. Infrared Thermography

IR thermography was performed using a calibrated FLIR A655sc MWIR camera to measure the surface temperature of the ramp. The camera has a resolution of 320 x 256 pixels with a frame rate of 200 Hz and an uncertainty of ±2° C (−40° − 150° C) or ±2% of the reading (100° − 650° C). To increase the signal-to-noise ratio of the IR measurements, the surface of the entire model was coated with a thin layer of Rust-Oleum™ High Heat black paint, resistant to temperatures up to 1200° F (649° C). The elastic modulus of the paint layer is orders of magnitude smaller than that of AMS 5659 steel, so the paint layer is expected to have a negligible impact on the panel response. Bench-top calibration of the camera with a 15-5 PH/H1025 coupon coated in the black paint gave an emissivity of $\epsilon = 0.92$. To verify the measurements from the infrared camera, two stick-on type-E thermocouples with a sampling rate of 50 Hz were placed on the lee-side of the rigid portion of the ramp.

E. Photogrammetry

Measuring the out-of-plane motion of a compliant panel in a hypersonic facility is a difficult task but extremely important for understanding the structural dynamics. Photogrammetry was chosen for the present experiments since it is a non-intrusive technique that allows for full-field deformation measurements. Modal-decomposition techniques then allow the active mode shapes and vibratory power contained within them to be resolved. In our setup, a grid of markers was painted on the exposed surface of the compliant panel. Since the IR thermography required the model to be painted black, the markers on the panel were painted using a thin layer of Rust-Oleum™ High Heat white paint. This allowed for simultaneous measurements of both the panel motion and surface temperature. To ensure circularity of the markers, we employed a stencil methodology similar to that of Whalen et al. [27]. Two 25 x 10 grids of 1.27 mm diameter circular markers were painted onto the panel with a 20.2 mm streamwise central strip separating the two grids, as shown in Figure 2. The purpose of the central strip was to allow for a wide enough interrogation area for the thermography in the case that the white markers interfered with measurements. Two columns of markers on each grid were painted onto the rigid portion of the ramp to act as reference markers for tracking the bulk model motion.

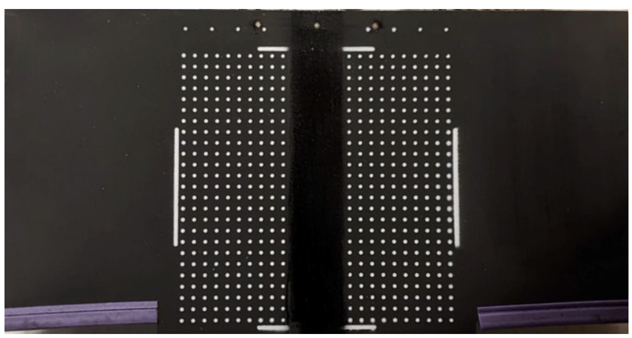

Fig. 2 Painted ramp with marker grid on the compliant region.

Four 613 nm Luminus PT-120 big-chip light emitting diodes were each passed through a condenser lens, parabolic reflector, and diffuser to illuminate the panel with focused, uniform light through the ZnSe window that was also used for the IR thermography. Above the test section, two Vision Research Phantom high-speed cameras, one v2512 and one v2640, were mounted to a cage on either side of the window such that the IR camera still had a direct line of sight to the panel. Both high-speed cameras were equipped with a Nikon Nikkor 60-mm lens; the v2512 imaged at a resolution of 768 x 768 pixels, whereas the v2640 imaged at 768 x 864 pixels. Both cameras collected images at 31 kfps using an exposure time between $10 - 20\mu s$; due to camera memory constraints, only approximately 2 seconds of run-time data were collected. The synchronized cameras sent a signal to the Dewetron DAQ so that it was known exactly when the cameras were triggered with respect to the other interrogation methods. The position of the markers in each image pair were determined using the highly accurate super-ellipse marker tracking algorithm developed by Duchene et al. [10]. Calibration of the two-camera apparatus was performed by imaging a 16 x 9 grid of markers on a hand-held plate at various orientations and using the bundle-adjustment algorithm provided by Walker et al. [35]. Such a calibration was done for each ramp angle, with typically 50 images from the synchronized calibration videos used to constrain camera parameters. Wind-off images of the painted panel were captured at vacuum conditions (with a vacuum on the back-side of the compliant region to give a Δp of 0 kPa) before each run to evaluate the possibility of plastic deformation occurring during the test campaign.

Once the marker motions were determined, we performed spatial Gaussian averaging (with $\sigma = 9.5$ mm) of the measured out-of-plane displacements, ω', in order to reduce measurement noise and account for variable paint thickness, while limiting attenuation of higher panel mode shapes and measurements of the spectral panel response power. By measuring the positions of the reference markers placed on the rigid panel housing, we are able to isolate any bulk motion of the plate due to model motion that occurs during the test time; this bulk motion is subtracted out from the displacement data of all the markers, allowing accurate measurements of the quasi-static and dynamic panel deformation. The accuracy of our photogrammetry routine is highly dependent on the camera separation, ramp angle, and flow state, as well as the marker-tracking accuracy. Laboratory calibration is inadequate for reproducing all of the test conditions; therefore, we performed an in situ estimate of the measurement error for each flow condition. Making use of the fact that no coherent panel motion is detected above 13 kHz, we high-pass filtered the time series data and make use of both Parseval's theorem and the assumption that measurement error is a white noise process to obtain the expected measurement error of each marker. The standard deviations of the filtered data were multiplied by five to represent a high-confidence bound on the measurement error, similar to in refs. [10, 27]. The mean out-of-plane displacement errors determined in this manner were of the order of $\bar{\omega'} = 3.1\mu m$; these errors were not found to vary significantly with θ.

III. Results

A. Incoming Boundary-Layer State

To begin, we briefly characterize the state of the incoming three-dimensional boundary layer produced by the half trips. A full picture of the upstream boundary-layer state following the flow trips is provided by the IR data on the flat-plate region from a previous campaign by ref. [36], reproduced in Figure 3. The flat plate of these experiments matched the dimensions in the present case; however, the entire flat plate was painted with Rust-Oleum black paint, which produced a blunting effect of the leading edge that slightly delayed transition on the flat plate. Nevertheless, the results on the boundary-layer state should remain qualitatively similar to the present experiments. The location of the pitot-rake in the presented image is at the same streamwise location as the ramp in the present experiments. We see clearly an elevated localized temperature on the tripped side of the plate, with a spread angle measured as $\theta_{\text{lat}} \simeq 4.5°$, indicating the onset of turbulent flow on the tripped side [37]. We also note that the turbulent flow does not spread past the centerline of the model upstream of the rake location, and thus the turbulent flow is localized on the tripped side of the plate.

To supplement the IR results, in Figure 4 we show the spectra of the pressure fluctuations along the spanwise extent of the panel in the upstream plate region. Spectra are taken from sensors at $x_c = -11.4$ mm along the model centerline and $y = \pm 5.7$ mm away from the centerline (the positive direction corresponds to the side of the boundary-layer trips) for the 10° ramp in the present flow conditions; additionally, we present the centerline spectrum for a fully untripped case as well as from a fully turbulent boundary layer, with flow conditions given by refs. [7, 28] (i.e., Condition B in each paper, with a free-stream unit Reynolds number of $23.6 \times 10^6\ 1/m$). As we will see, the upstream boundary layer was unaffected by the SWBLI for this ramp angle. The power spectral density (PSD) were calculated using Welch's method, averaging 10,000-point segments of the pressure signals with 50% overlap. We first note the spectra along the centerline for the tripped (T) and untripped (U) cases, as well as the spectra taken from the tripped experiments at $y = -5.7$ mm off the centerline (away from the trips), are all overlapping. The spectrum taken at $y = 5.7$ mm off the centerline (towards the trips), however, nearly matches the spectrum taken at the centerline for a nominally turbulent incoming boundary layer. These results indicate the trips introduce a localized turbulent flow which does not extend to (or past) the plate centerline at this location downstream. We thus expect the development of a three-dimensional SWBLI, producing asymmetric aero-thermal loading on the compliant region.

B. Underlying SWBLI Flowfield

To better contextualize the later FTSI results, we now provide a brief characterization of the underlying SWBLI flowfield and the dynamic pressure loading for the various ramp angles. For the off-surface flowfield characterization, we rely on schlieren visualizations made on the compliant ramp configuration; we note some degree of surface vibrations will be present in these data; however the amplitude of these vibrations is too small (as we will see) to introduce meaningful changes to the basic flow structures in the schlieren. We note also that the focusing schlieren effectively visualizes a narrow slice about the mid-plane of the flat-plate/ramp; considering the three-dimensional nature of the

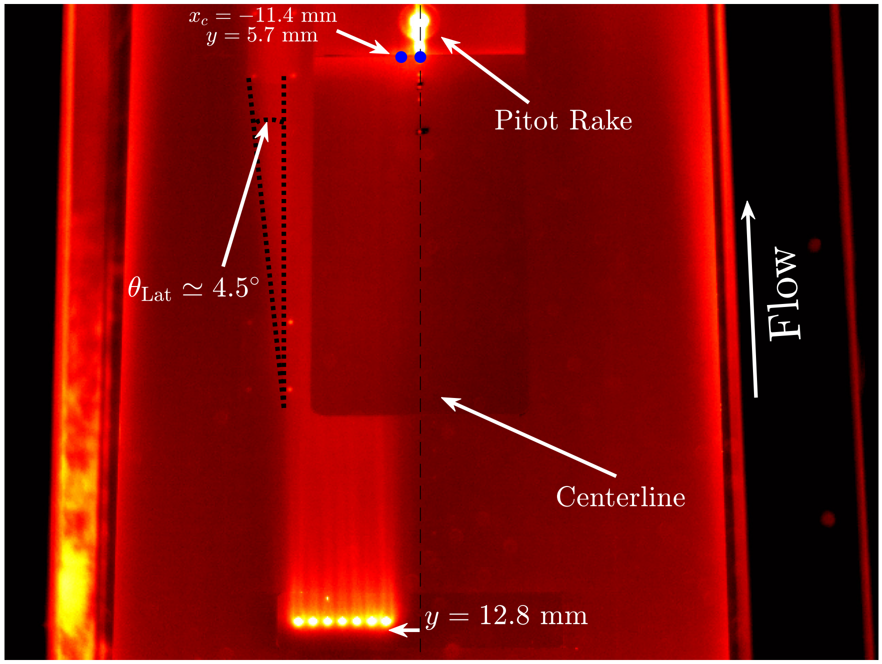

Fig. 3 IR Image of the tripped boundary layer on the flat plate in a previous pitot-rake study by ref. [36].

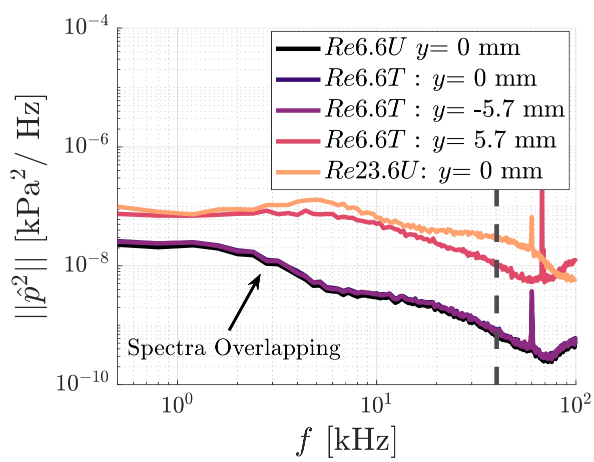

Fig. 4 Spectral development of sensors at $x_c = -11.4$ mm at the centerline and ± 5.7 mm off the centerline for $Re_\infty = 6.6 \ 10^6/m$ and $\theta = 10°$. Spectra also shown for experiments without boundary-layer trips (denoted in the legend with the U) for nominally transitional and turbulent Reynolds numbers. The designator y_5 represents the sensor that is 5.7 mm off the centerline in the direction of the boundary-layer trips.

SWBLI (and incoming boundary layer), this will not be necessarily representative of the full flowfield.

In Figure 5, we provide sample background normalized schlieren images for each ramp angle, with maroon points indicating the location of Kulite sensors The ramps are seen to experience varying degrees of boundary-layer separation, spanning from fully attached at $\theta = 10°$ (and possibly 20°), to weakly separated at 30°, and fully separated for the higher ramp angles. For all ramp angles there are noticeably turbulent structures visible, and for the separated SWBLIs we see this turbulence extending into the shear layer, especially near the corner region. The presence of these turbulent structures, even for the 10° case where we expect transitional flow along the centerline, indicates we are seeing some line-of-sight integrating effects from the narrow depth of focus of the SAFS setup. For the separated SWBLI cases, we also see highly curved disturbances like those observed in Whalen et al. [7]. As the extent of the separated flow region

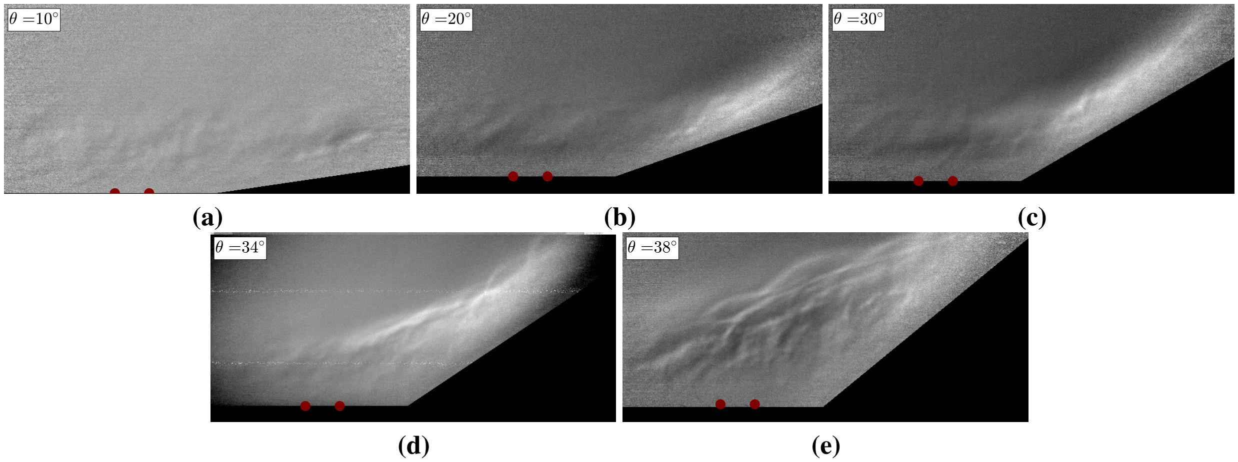

Fig. 5 Representative mean-normalized focusing schlieren images of (a) $10°$**, (b)** $20°$**, (c)** $30°$**, (d)** $34°$**, and (e)** $38°$ **ramps. The maroon marker denotes the sensor locations for Figure 8.**

grows, the separation location moves upstream and the reattachment location downstream. To compare the overall nature of the flow fluctuations for the different compression angles, we employ Spectral Proper Orthogonal Decomposition (SPOD) on the focusing schlieren data, making use of the SPOD routine provided by Towne et al. [38]. This algorithm determines a set of orthogonal modes for each frequency based on an eigendecomposition of the cross-spectral density tensor formed by Fourier-transformed images. Compared to proper orthogonal decomposition (POD), which produces modes that are coherent only in space, SPOD is able to construct modes that are coherent in space and time, thus representing dynamically significant features of the selected process. Figure 6a shows a comparison in the energies of

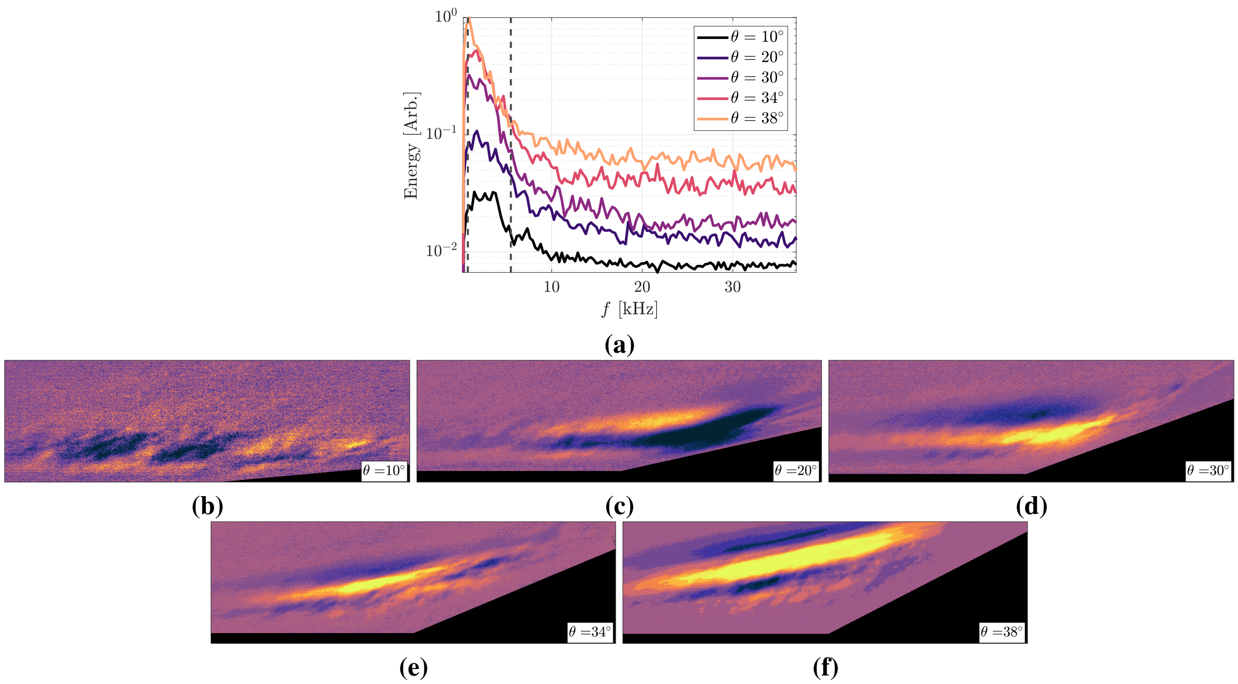

Fig. 6 (a) SPOD highest-ranked mode energy of focusing schlieren data for each compression angle (note the vertical dashed line represents the upper bound for anticipated natural frequencies of the compliant panel). (b-f) Associated energy maps obtained by integrating the SPOD signal between $0.5 \leq f \leq 5.5$ **kHz for each ramp angle.**

the highest-ranked SPOD mode for each ramp angle, normalized by the maximum value of the 38° curve. We present data only from the highest-ranked mode here, as it represents the greatest energy content and captures the dominant fluid features. Clearly, for each ramp angle, there are elevated fluctuation energies in the range of frequencies associated with the compliant panel natural motion ($f \lesssim 10$kHz) and the stronger SWBLIs elevate the overall power of these fluctuations. Combined energy maps obtained by integrating the SPOD signal between $0.5 \leq f \leq 5.5$ kHz are presented in Figure 6b-f, showing the concentration of flowfield energy most relevant to the natural structural motion of the panel. This low-frequency unsteady fluid motion is expected to be capable of exciting and coupling with vibrations of the compliant panel region. The concentration of this low-frequency energy appears to lift away from the plate/ramp surface as the ramp angle is increased, likely due to the increased separation lengths of the higher ramp angle experiments elevating the shear layer of the incoming SWBLI; this will significantly change the mean impingement location of the flow on the compliant region and potentially alter which natural modes of the panel are most excited.

The spatial distribution of the mean and temporally varying wall pressure upstream of the corner gives further insight into the nature of the hypersonic SWBLI. The normalized mean pressures and RMS fluctuation values over the full test time from the centerline Kulite sensors are presented for each ramp in Figure 7. Only frequencies less than 40 kHz were used in the evaluation of the RMS fluctuation values shown. Here we normalize the sensor streamwise measurement locations by the nominal untripped transitional boundary layer height, δ_0, on the flat plate, informed by ref. [39]. For the mean pressure (Figure 7a), the 10° and 20° ramp values remain essentially constant, confirming that the flow remains attached until the most downstream sensor ($x_c = -7.6$ mm). For the other three ramp angles, we see a significant rise in the pressures as the flow approaches the compression corner. As we would expect, the higher ramp angle produces a larger pressure rise and an extended region of upstream influence: the 30° ramp begins to show an increase in $\bar{p}/p_\infty$ away from unity at $x_c = -22.8$ mm ($x_c/\delta_0 = -1.65$), indicating this is potentially where the flow is beginning to separate. A similar increase occurs further upstream than any of the measurement locations for the 34° and 38° ramps, showing their increased separation regions. The normalized RMS pressure variations (Figure 7b) show similar trends to the mean pressures, though the higher ramp angles ($\theta \geq 34°$) exhibit a plateau region approximately $\sim 2.5\delta_0$ upstream of the corner, similar to trends observed in ref. [7]. Comparing these results to measurements on the untripped geometry by Schöneich et al. [28], we see these centerline pressure profiles are fairly similar for the lesser ramp angles ($\theta \leq 30°$), indicating the flow along the centerline is mostly unaffected by the increased turbulence of the tripped flow for these ramp angles. However, for the higher ramp angles, we note a modest reduction in the mean pressure rise in the streamwise direction and slightly elevated levels of RMS pressure variations along the centerline, indicating the larger separated flow region allows turbulent flow from the tripped side to travel in the spanwise direction.

To give a more detailed understanding of the structurally relevant pressure loading content on each ramp, in Figure 8(a,b), we show the spectra of the pressure fluctuations for the two centerline ($y = 0$) transducers closest to the corner for each ramp angle, revealing the pressure loading conditions that could induce vibrations in the compliant panel. Additionally, spectra for the two transducers at $x_c = -11.4$ mm and $y = \pm 5.7$ mm away from the centerline (the

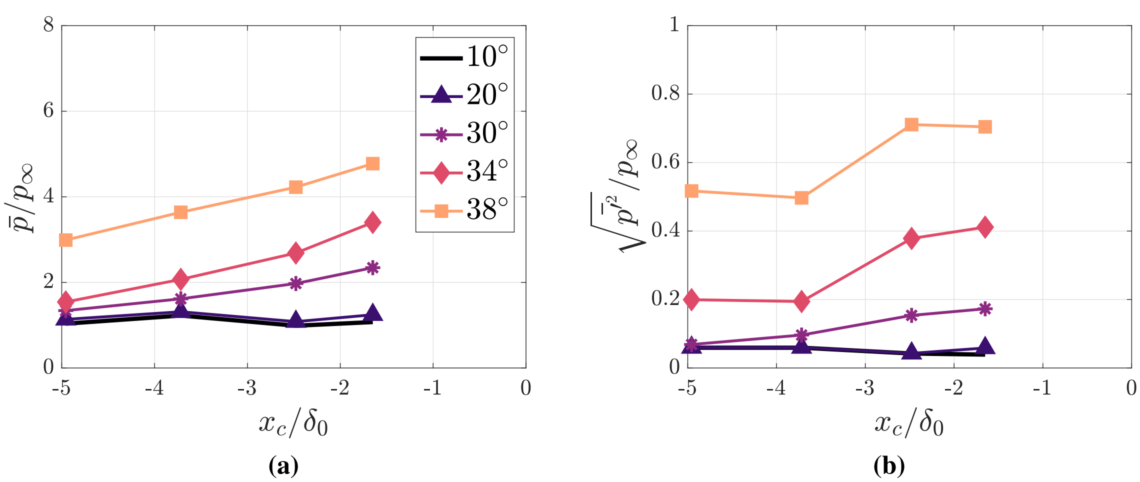

Fig. 7 (a) Mean pressure measurements and (b) RMS pressure measurements, normalized by the free stream pressure, on the upstream flat plate for each ramp angle, θ.

positive direction corresponding to the side of the boundary-layer trips) are presented in Figure 8(c,d). Again, the PSDs were calculated using Welch's method, averaging 10,000-point segments of the pressure signals with 50% overlap. Comparing first the centerline sensors' spectra in Figure 8a and b, there is a generally consistent shape in the PSD for all ramp angles, with a largely monotonic increase in fluctuation energy and an increased region of elevated powers in the frequency range of the primary structural response for larger ramp angles. We do note that, for the further upstream sensor ($x_c = -11.4$ mm) in Figure 8a, the spectra of the 10° and 20° are near identical, and it is not until further downstream at $x_c = -7.59$ mm (Figure 8b) that the 20° ramp produces signs of intermittent separation and increased unsteadiness. The similarity in the spectra for the $\theta \geq 30°$ ramps between the two sensor locations is indicative of the relatively large separation length scales experienced at these compression angles. Looking now at the sensors offset from the model centerline, the sensor away from the boundary-layer trips (Figure 8c) exhibits spectra that are nearly identical to those of the sensor on the centerline at the same streamwise location (Figure 8a). We note the larger ramp angles ($\theta \geq 34°$) seem to show a slightly extended region of elevated low-frequency ($f \lesssim 8kHz$) power, indicative of turbulent information traveling in the spanwise direction of the separation region. However, in the spectra of the sensor on the tripped side (Figure 8d), we see clear elevated power levels for all ramps; this would indicate that the higher levels of turbulence induced by the boundary-layer trips have not yet spread (or in the case of the larger ramp angles has only slightly spread) to the model centerline by this location downstream. Thus, the tripped side of the plate and ramp can be expected to experience increased levels of heating, thus reaching higher surface temperatures earlier on in the test

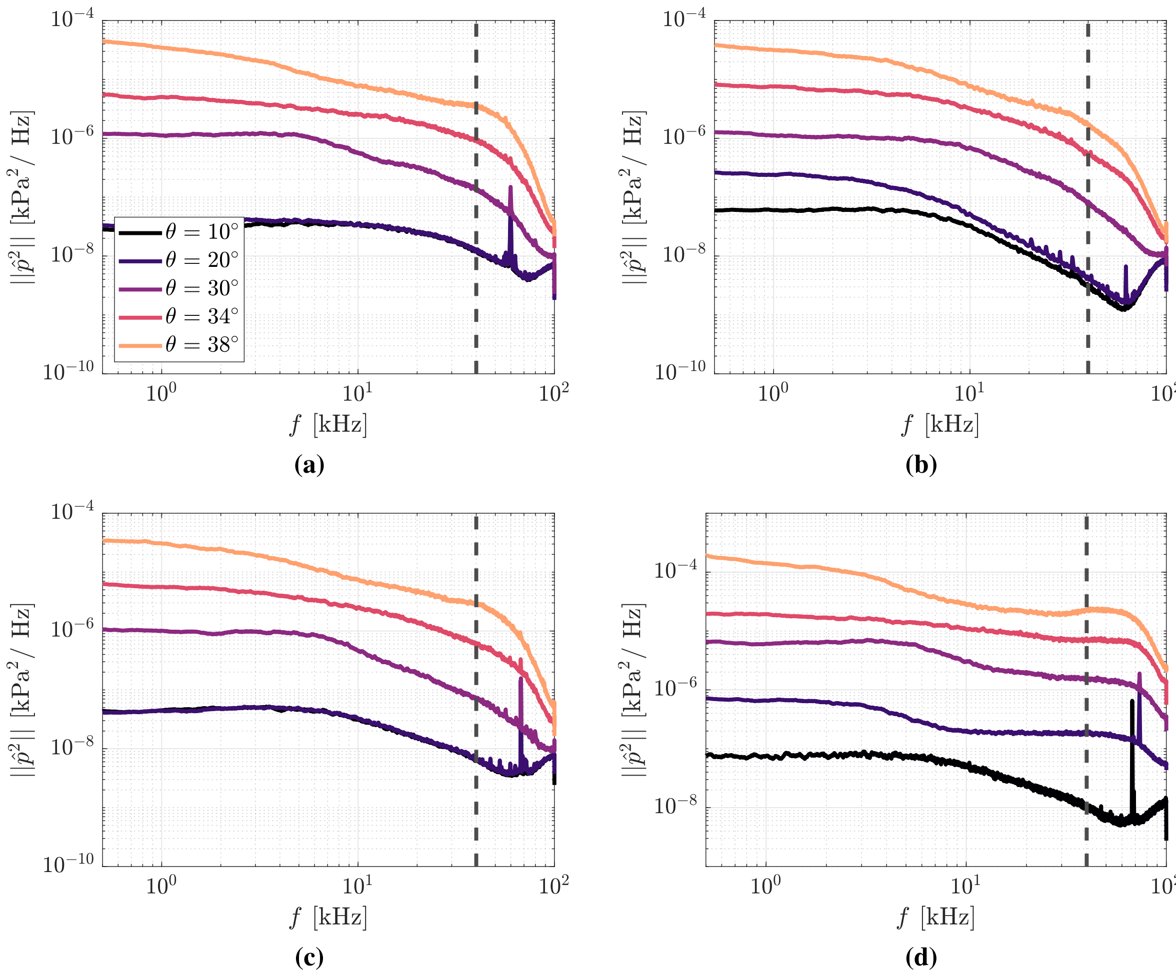

Fig. 8 (a,b) Spectral development of sensors at $x_c = -11.4$ and -7.59 mm**, respectively, along the plate centerline** ($y = 0$) **for varying ramp angles. (c-d) Spectral development of the sensor at** $x_c = -11.4$ mm **and** $y = \pm 5.7$ mm **offset from the centerline (c) away from and (d) towards the boundary-layer trips.**

time. This could result in a non-uniform spanwise thermal strain distribution, which could significantly alter the panel's dynamic structural motion.

C. Surface-Temperature Measurements of the Compliant Panel

We now assess the thermal state of the compliant region along the ramp. Knowledge of the thermal state of the panel is fundamental for understanding the thermal effects on its structural dynamics. Previous studies at hypersonic conditions have indicated a significant influence of the panel temperature, with resulting static deflections an order of magnitude larger than the panel thickness and notable shifts in the vibrational frequencies of different panel natural modes [10, 27, 28]. In Figure 9, we present the surface temperature measurements one second after the photogrammetry cameras begin recording (approximately 3-4 seconds after model injection), taken on the compliant ramp configuration for each ramp angle. The compliant panel region is consistently at an elevated temperature relative to the rest of the rigid ramp body due to the disparate thicknesses of the regions. For all the separated SWBLI cases ($\theta \geq 30°$), an enhanced heating region develops near the corner of the ramp, progressing downstream as the ramp angle increases. We expect the zone corresponding to the peak temperature increase to lie at or near the SWBLI reattachment region on the ramp [24, 28, 40]. For each ramp, we also note that the spanwise temperature distribution is non-uniform, with elevated heating on the side of the flow trips (the left side of each image). For the $\theta \geq 34°$ ramps, the streamwise peak-heating region on the tripped side of the panel lies noticeably upstream compared to the peak on the non-tripped side, indicating that the more-turbulent nature of the tripped flow causes a compressed separation region.

Noting that the panel temperature distributions show both streamwise and spanwise variations, we now compute the time-resolved centerline and $x/L = 1/3$ span-line temperature profile for each ramp angle. The resulting spatio-temporal distributions, shown in Figure 10, provide insight into the time evolution of the streamwise and spanwise temperature profile of the ramp; the horizontal dashed lines in the contours correspond to the beginning and end times of the

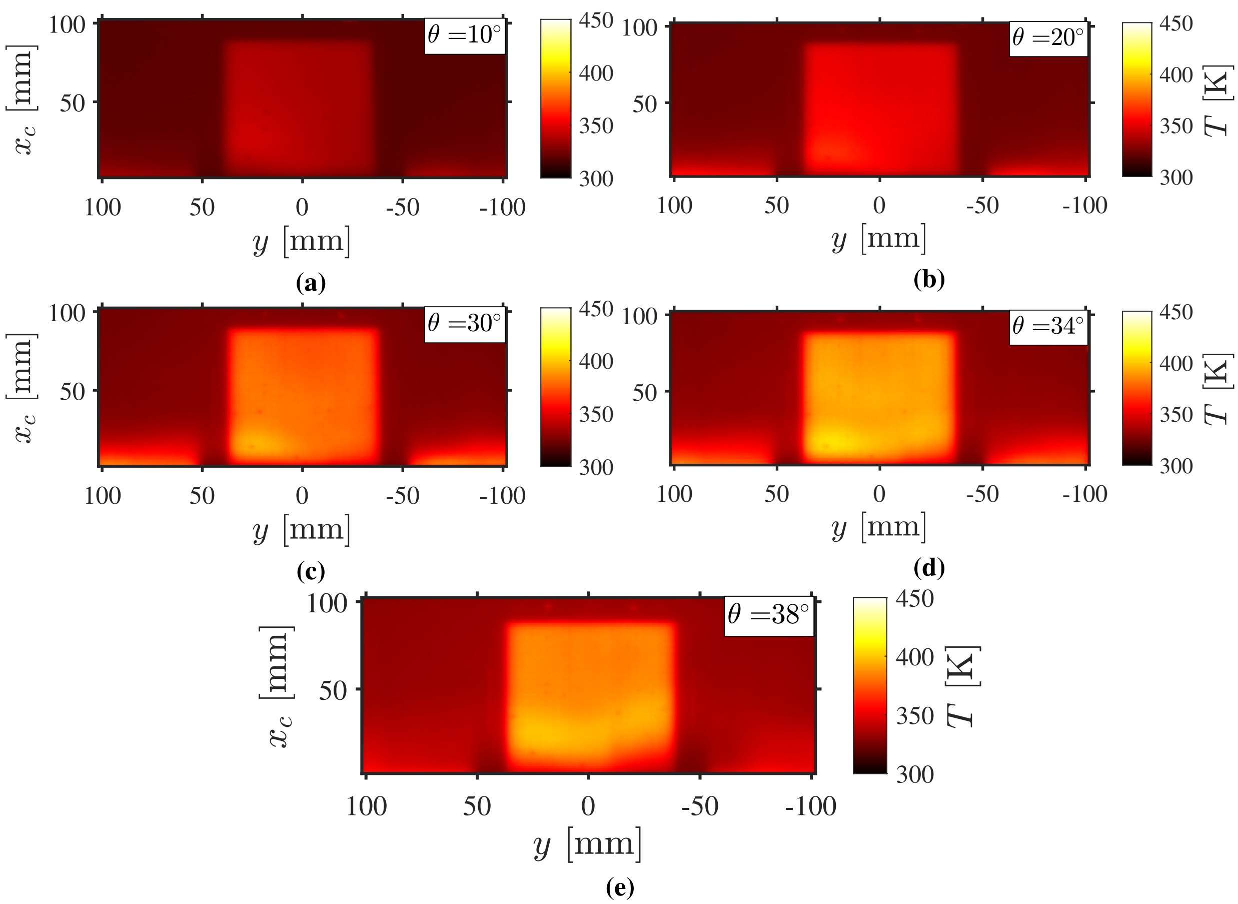

Fig. 9 IR surface temperature measurements at t = 5 seconds for each ramp angle.

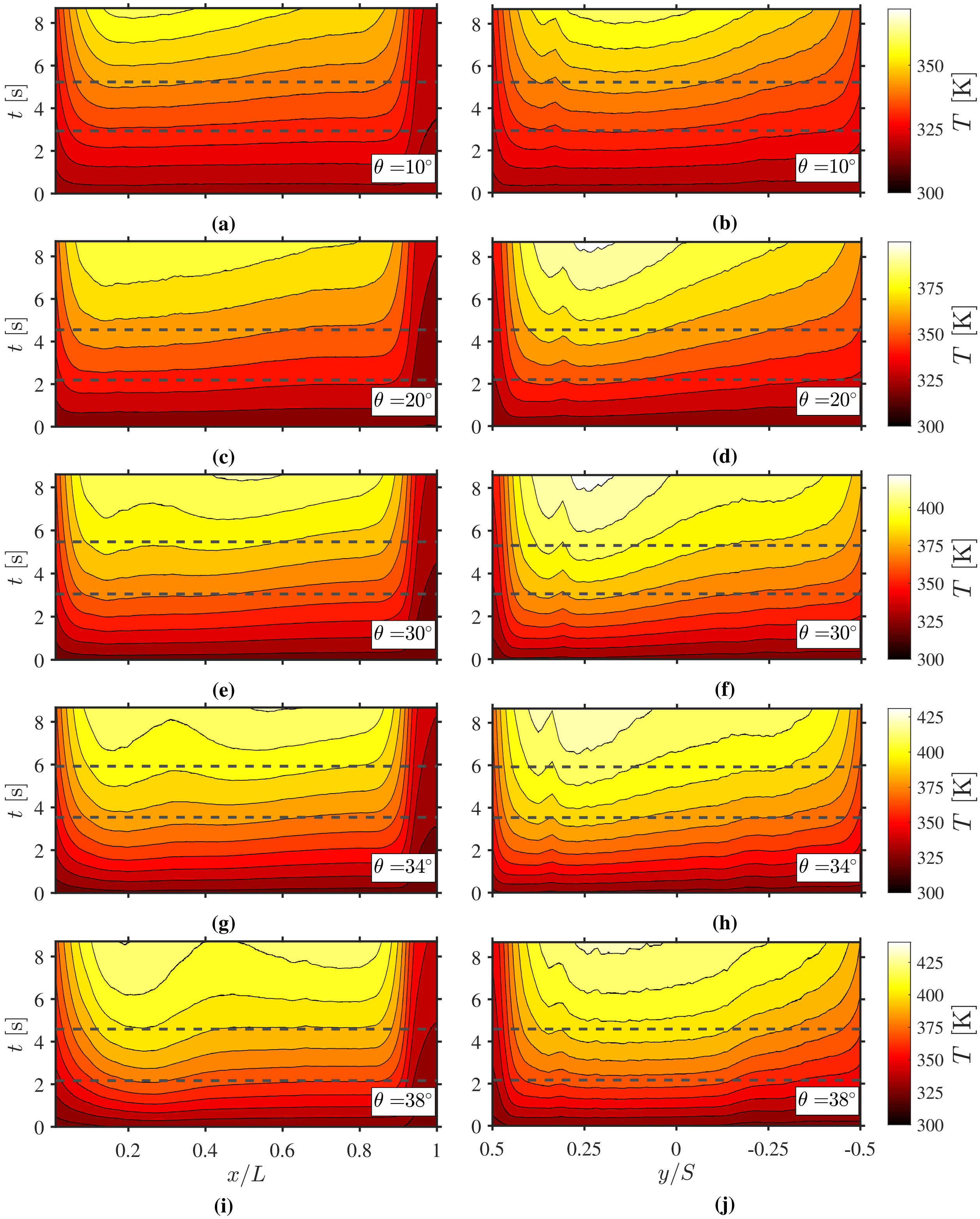

Fig. 10 Spatial-temporal surface temperature distributions along the (a,c,e,g,i) centerline and (b,d,f,h,j) spanwise distribution along $x/L = 1/3$, for each ramp angle.

photogrammetry data. We note a consistent temperature rise at all locations throughout the test time for each ramp angle, indicating that the local adiabatic wall temperature has yet to be reached anywhere on the panel. In Figure 10a, the unseparated $\theta = 10°$ ramp displays a peak heating region near the corner between $0.15 \lesssim x/L \lesssim 0.3$, followed by a region of decreasing surface temperature; for $\theta = 20°$, the contours have a similar shape, but at elevated temperatures. For the fully separated cases ($\theta \geq 30°$), there is a noticeable initial peak followed by a cooler region, with a (typically) weaker secondary peak developing toward the end of the test time. Both the peak heating region and the intermediate trough move downstream with increasing θ. The maximum final surface temperatures achieved during the photogrammetry recording time range from $T \simeq 350$ K for the 10° ramp up to $T \simeq 425$ K for the 38° ramp. The local elastic modulus, E_T, of the material depends on the material temperature and, for the present stainless steel, E_T will decrease with rising temperatures; for the surface temperatures realized here, the local elastic modulus will be reduced by up to 3.5%.

For the spanwise spatial-temporal distributions in right column of Figure 10, the positive y/S (tripped) side of the panel heats up consistently more quickly due to the more turbulent nature of the localized flow. This effect seems to be similar for all ramp angles, with $y/S \simeq 0.25$ generally corresponding to the area of maximum heating. The spanwise temperature differences tend to increase with time; during the photogrammetry recording period, temperature differentials of up to 15 K are realized for the higher ramp angles. The higher temperatures experienced on the tripped-side of the panel will likely lead to larger changes to the temperature-dependent material properties, which can in turn be expected to alter the localized panel dynamics.

The temperature differential between the compliant region and its rigid support is also important as it will cause enhanced thermal stresses that can modify the panel response. For each ramp angle, we thus compute the mean temperature difference, $\bar{\delta T}$, along the streamwise direction (taken at $y/S = 0.25$, i.e., midway across the tripped half) between the compliant panel and the rigid part of the ramp (tripped side), with results shown in Figure 11. We see that $\bar{\delta T}$ increases monotonically but at a diminishing rate with time, especially for the higher ramp angles. This later time behavior indicates that the compliant panel is beginning to approach the adiabatic wall temperatures, while the thicker rigid support is still being heated. Near the end of the test time, this maximum temperature difference ranges from 32 K for the 10° ramp to 70 K for the 38° ramp. The spatial-temporal streamwise distributions of this $\bar{\delta T}$ (not shown) follow the same form as those seen in the left column of Figure 10.

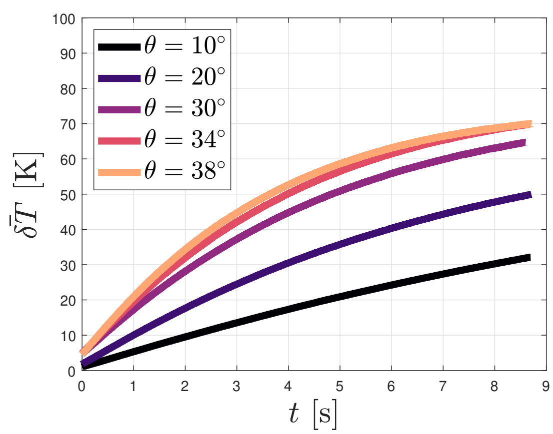

Fig. 11 Time-varying difference between the average streamwise surface temperatures of the tripped compliant panel region and the supporting rigid ramp for each ramp angle.

Knowledge of the thermal loading and likely mode shapes can provide early insights into which panel natural modes are most likely to be affected by the changing thermal environment. We employ the method of Young [41] to define a set of analytical mode shapes based on the products of the clamped-clamped beam solution, which allows us to determine the antinode locations for the theoretical mode shapes. Hereinafter, we use the standard (m,n) naming convention for the panel natural mode shapes, where m designates the number of antinodes in the streamwise direction and n the number in the lateral direction. We note the regions of large δT occur between $0.1 \lesssim x/L \lesssim 0.4$, which fall near the front-most antinode locations of the (2,1), (2,2), (3,1), and (3,2) mode shapes, suggesting that these modes are most likely to experience changes during the test time. The asymmetric spanwise temperature profiles indicate disproportionate heating near the (m,n≥2) antinode locations, which may manifest itself in local panel dynamic alterations between the tripped and non-tripped sides. In general, two competing effects are produced by the thermal loading: 1) increases in δT between the panel and the support will yield increased thermal strains and thus affect panel dynamics in a similar manner to a pressure differential; 2) as noted above, increased panel temperatures will lead to a reduction in the modulus of elasticity in an effect known as thermal softening, which tends to reduce the natural frequencies and can enhance vibrational response. Meanwhile, the panel will experience quasi-steady static deflections due to the compressive and thermal strains. This induced curvature in the panel has been shown to reduce vibrational response, increase natural frequencies, and even alter the spatial distribution of the panel natural modes [10, 27, 28].

D. Time-Averaged Dynamic Response of the Panel

Now moving to the photogrammetry measurements, to understand how the panel dynamics change for the different ramp angles, we first compare the modal responses of the panel at selected conditions. We make use of the SPOD routine applied to the out-of-plane displacements of the grid markers to identify the vibrational frequency and shape of excited panel modes [38]; Figure 12a compares the spectra for select ramp angles, and Figures 12b through 12j show the first nine active mode shapes for a 38° ramp experiment (indicated by the red dots in Figure 12a). Here, we only examine the first 0.3 seconds of the photogrammetry data for each run; the reasoning for this is that (as we show later) significant frequency shifting occurred throughout the test due to the changing panel state, which obscures direct comparison of the spectral data. Beginning with Figure 12a, we see quite clearly that, as the ramp angle increases (and thus the SWBLI strength), a greater number of panel natural modes are excited. This can be attributed to the higher levels of unsteady fluid motion impulsively loading the panel at multiple antinode locations. For all tests in which the flow was separated approaching the ramp corner, a significantly increased number of vibrational modes were excited compared to non-separated flow cases. The maroon ticks in the top of Figure 12a represent the wind-off frequencies presented in Table 2; we see that under the SWBLI loading the modal vibrations lie at somewhat higher frequencies than expected, which as we will see is likely due to the non-zero quasi-static deflection present. Looking now to the mode shapes present in Figure 12b-j, we see that these generally conform to those expected in classical flat plate theory. The blank strip down the centerline prevents us from fully resolving the panel motion; nevertheless, the nature of most of the mode shapes present can be inferred from the available measurement and our knowledge of the natural panel modes. The first four modes clearly represent the (1,1), (1,2), (2,2), and (3,1) mode shapes; these four modes were generally activated in all tests. We note some interesting effects occurring with the (1,2) mode; the spatial distribution is not entirely similar to the theoretical prediction, with the antinode location near $y/S = 0.2$ skewed upstream on the panel. The (1,1) and (2,2) modes also show slight asymmetries, with the modal displacements on the tripped side of the panel being displaced slightly upstream as well. These antinode peaks correspond to the peak heating location in the spanwise temperature distribution shown in Figure 10j, likely indicating that the higher temperature on the tripped-side of the panel causes augmented deformation and vibrational shifts to the local structural dynamics. The fifth mode shape shown (Figure 12f) most likely corresponds to the (1,3) mode, with spanwise varying antinode peaks, though some uncertainty remains in this conclusion. The sixth through ninth distributions (Figure 12g-j) all exhibit higher order natural mode shapes, which most likely represent the (3,2), (2,3), (4,1), and (3,3) modes, respectively.

To assess the effects of the flow asymmetry on the panel motion, we compare the SPOD spectra of the $\theta = 30°$ and 38° cases with the half-trips engaged to the corresponding untripped case, as shown in Figure 13. In the spectra shown, red circles are used to denote the peaks corresponding to modes with spanwise aligned antinodes, as we expect these to differ the most in response to the asymmetric SWBLI loading. We first note the overall reduced responses for the tripped flow cases, as these cases experienced slightly higher levels of quasi-static deflection and the induced curvature acted to dampen vibrational response. However, we see that the reduction in λ_k at frequencies corresponding to modes with spanwise antinodes is lesser than for modes with streamwise aligned antinodes. For both ramps, the (3,1) modal response near $f \simeq 1.85$ kHz and the (4,1) response near $f \simeq 3$ kHz are heavily dampened for the tripped-flow cases; however, the (m,n>2) modes show λ_k values that are near to (or in some cases greater than) the spectrum corresponding to the untripped cases. This seems to indicate that the asymmetric loading in the present case is more likely to activate and sustain excitation for spanwise varying mode shapes, as compared to a fully two-dimensional SWBLI.

As we have mentioned, due to the aero-thermal loading on the panel and the disparate thermal masses between the rigid ramp and thin compliant region, significant thermal stresses (as well as normal stresses from any pressure differential present) will cause the mean panel geometry to change. For the given fully-clamped plate, the maximum quasi-static deflection is expected to occur at/near the centerline. To estimate the deflections there from the photogrammetry measurements (given the absence of markers near the centerline), we perform quadratic interpolation to estimate the in-plane position of centerline surface elements and subtract out the in-plane position of the fixed markers. The

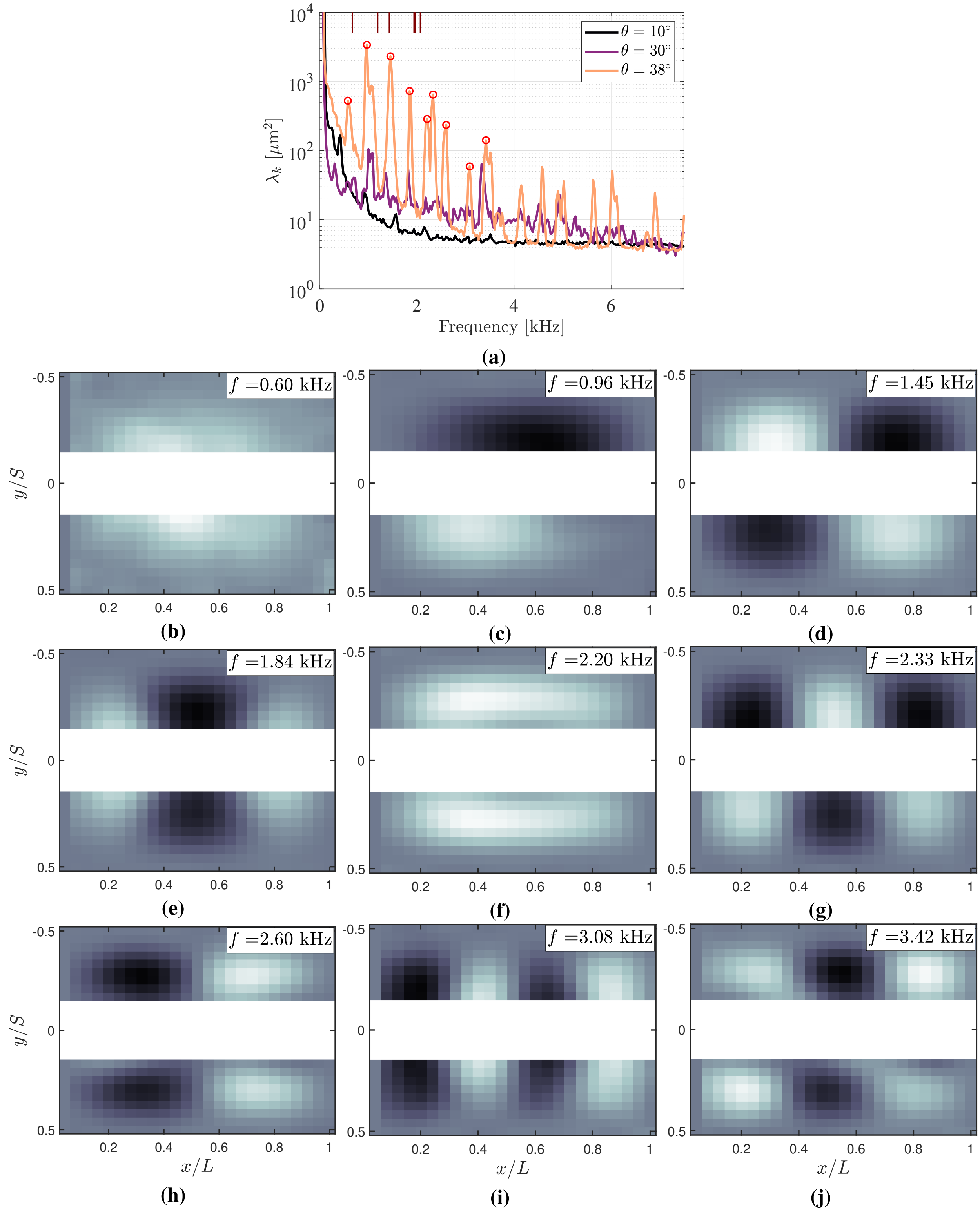

Fig. 12 SPOD spectra for the 10°, 30°, and 38° ramp angles (the red circles denote the frequencies of the presented mode shapes). (b-j) Spatial distribution of first nine active mode shapes from θ = 38° ramp.

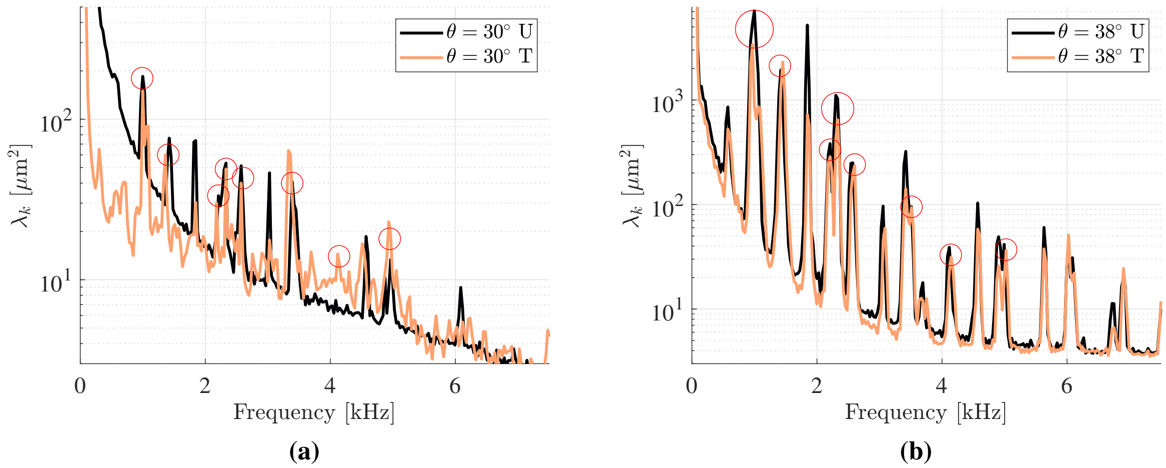

Fig. 13 SPOD spectra for the (a) 30° and (b) 38° ramp angles for the present asymmetric flow case and the transitional untripped flow case. The red circles highlight the frequencies corresponding to mode shapes with spanwise aligned antinodes.

maximum static deflection in a given experiment, ω'_{max} (where positive ω'_{max} indicates deflection inward to the ramp), can be computed as a function of time and then related to the temperature difference between the compliant panel and the rigid ramp, δT, as this latter quantity characterizes the degree of thermal stresses present. Figure 14 thus shows the maximum deflection for each ramp angle as a function of this temperature difference. In most cases, we see a finite initial deflection, followed by a further increase during the measurement time; the one exception is the $\theta = 10°$ ramp which shows a near-zero initial deflection and a period of temperature rise during which the deflection remains essentially unchanged. When present, the initial deflection can be attributed to the accumulated thermal stresses between the injection of the model and the beginning of the recording time (usually ~ 3 seconds). The maximum deflection of the larger ramp angles ($\theta \geq 34°$) deviate somewhat from trends established by the lesser ramp angles, producing somewhat reduced deflections, especially noticeable in the range of 35 K $\lesssim \delta\bar{T} \lesssim$ 50 K. The likely explanation for this is the pressure distribution on the panel differs significantly from the inviscid value (which was used to determine the cavity pressure necessary to give a nominal zero pressure differential across the panel) for these highly separated cases. We do, however, note the rate of change in ω'_{max} is higher for the larger ramp angles; this can be explained by the panel curvature reaching a point where nonlinear dynamics (such as membrane stretching) begin to dominate the deflection

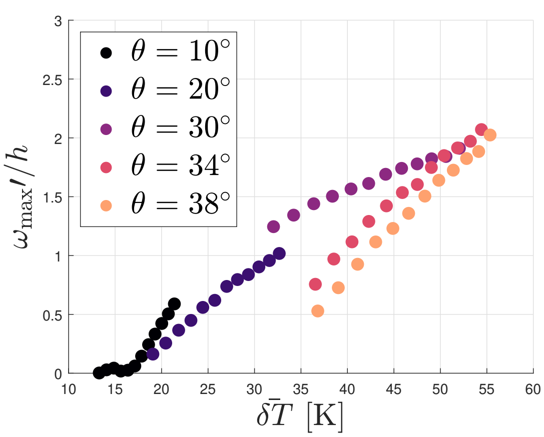

Fig. 14 Maximum static deformation normalized by panel thickness, h, as a function of $\delta T_{\text{Compliant-Rigid}}$ for each ramp angle.

behavior [42]. As is shown next in Figure 15, the deflection behavior appears asymmetric (more noticeably for the higher ramp angles) with slightly elevated deflections on the tripped side of the panel, explaining the asymmetries observed in some of the mode shapes with spanwise aligned antinodes.

The changes to the underlying panel geometry just noted motivates the calculation of the quasi-static von Mises stress field on the plate surface; this stress field, $\sigma(x, y)$, was obtained from the displacement field, $\omega'(x, y)$, by applying classical thin-plate theory under small-strain assumptions. Surface curvatures were computed from the second spatial derivatives $\omega'(x, y)$, and bending strains at the surface were evaluated using the Kirchhoff-Love kinematic relations. The strains were then converted to stresses using linear elastic plane-stress constitutive relations with the local temperature-dependent Young's modulus and Poisson's ratio of the material. The equivalent von Mises stress distributions, as well as the displacement field, are shown in Figure 15 for both the 10° and 38° ramp at the end of the recording period. Clearly, as the inward deflection of the panel increases, the surface stresses intensify and thus the stiffening effects on the vibrational response are expected to be amplified. We see local maxima in the stress distribution occur near the center of the panel and in an outer ring that passes through the (1,2) and (2,1) antinode locations. For the 38° ramp (Figure 15d) we see the stresses are elevated on the tripped side of the plate, due to the slightly asymmetric displacement shape. One might predict from the shape of this distribution that the quasi-static displacement should produce mode-dependent local stiffening, preferentially enhancing stiffness for certain modes (particularly those with antinodes near stress peaks).

To assess whether this prediction holds, we estimate the level of localized stiffening contained within each mode's nodal confines by integrating the $\sigma(x, y)$ distribution over the relevant modal area. This gives the quantity $\bar{R}_{\sigma}^{(\mathrm{m,n})}$,

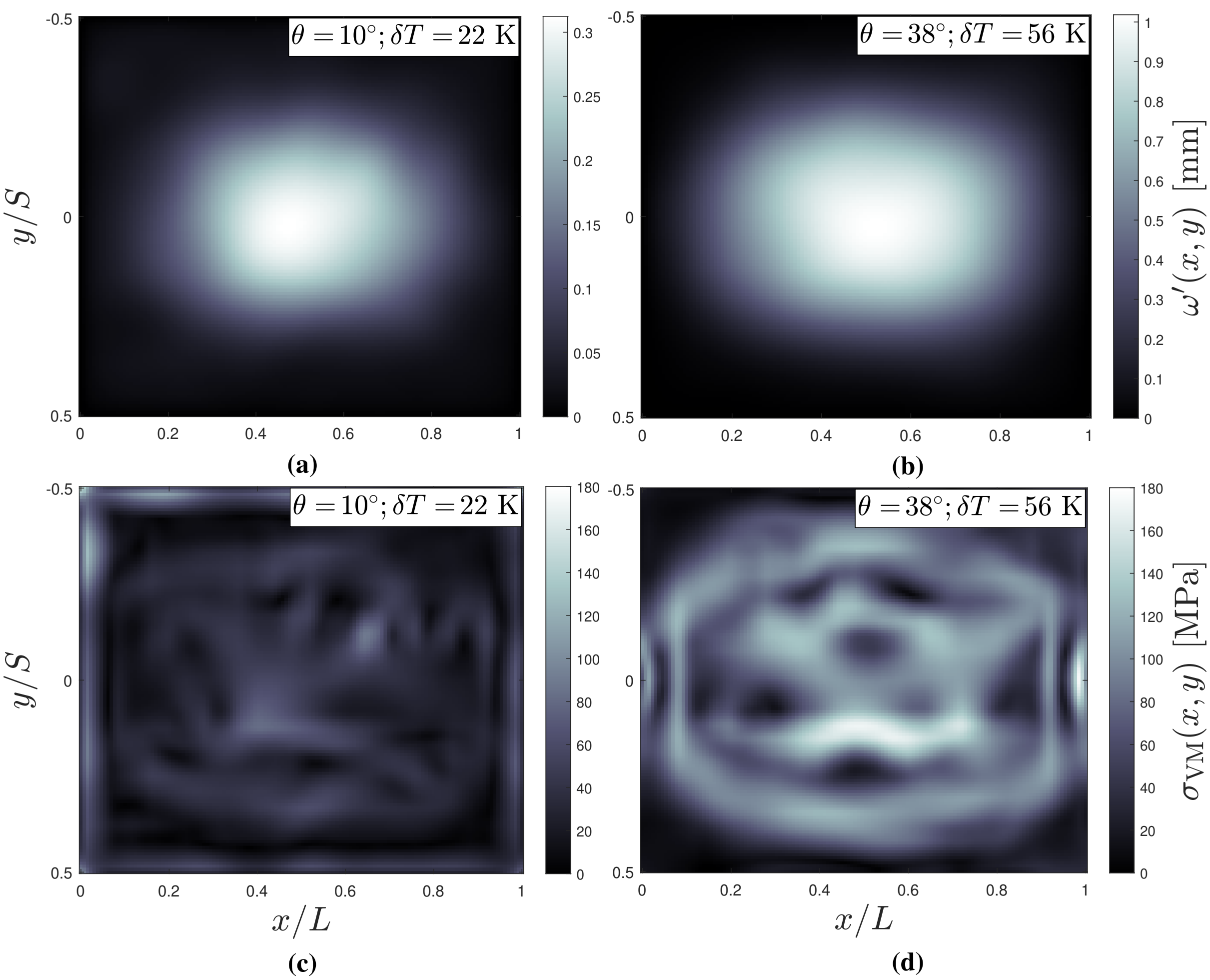

Fig. 15 (a-b) Final displacement field, $\omega'(x, y)$, for θ = 10° and 38° tests and (c-d) the respective surface von Mises stress distributions, $\sigma(x, y)$.

defined by

$$\bar{R}_{\sigma}^{(\mathrm{m,n})} = \int \frac{\sigma(x,y)\mathrm{dA}}{\mathrm{A}^{(\mathrm{m,n})}}, \tag{1}$$

which, when normalized by the material Young's modulus, we hereinafter refer to as the modal stress factor. Here (m,n) designates the mode and $\mathrm{A}^{(\mathrm{m,n})}$ is the area contained within the nodal lines of this mode. In computing the integral we assumed a constant $\sigma(x, y)$ over a rectangle around each marker, where the dimensions of the rectangle, dA, are given by the marker spacings (i.e., 3.58 × 3.53 mm). These modal stress factors are plotted against the time-resolved maximum quasi-static displacement in Figure 16a. All modal stress factors are observed to grow monotonically with displacement. The three lowest-frequency modes - (1,1), (1,2), and (2,1) - contain the highest levels of internal stress, and are thus expected to be the modes most influenced by stiffening effects that cause an increase in vibrational frequency, f. Conversely, the (2,2), (2,3), and (3,2) modes are all active in regions of the panel that contain relatively small levels of internal stress, and thus might be expected to be more significantly influenced by thermal softening effects which tend to reduce vibrational frequency. The remaining three modes presented - (1,3), (3,1), and (4,1) - all encompass regions of moderate stress, suggesting that they will be susceptible to both stiffening effects from induced curvature as well as softening effects from elevated surface temperatures. In Figure 16b, we present the normalized local elastic modulus averaged over the surface elements confined within the given mode's nodal lines (normalized by the nominal elastic modulus of AMS 5659 stainless steel) against the ramp-panel temperature differential, $\bar{\delta T}$; the local elastic modulus is derived from the temperatures obtained from the IR measurements. Here we present data only for the largest temperature differential measured as it shows the greatest spread in $\bar{E}_T^{(\mathrm{m,n})}/E_0$ between the different modes. The average modal elastic modulus is used as a proxy for the degree of local thermal softening across the panel, since the asymmetric streamwise and spanwise heating profiles observed in Figures 9 and 10 suggest certain modes lying in relatively hot regions of the panel will experience a stress alleviation from the lower local elastic modulus. We can see from Figure 16b that $\bar{E}_{\mathrm{T}}^{(\mathrm{m,n})}/E_0$ decreases with heating and the modes with spanwise aligned antinodes typically show the greatest reduction in elastic modulus due to the axisymmetric heating. This leads us to expect that the transient behavior of these modes - (2,2), (2,3), and (3,2) - will be more influenced by the thermal softening effects, as compared to the other selected modes. Ultimately, these relatively large (and temporally varying) panel deformations and panel stresses can be expected to have a significant influence on the panel mode shapes and dynamic response (see, for example, refs. [10, 43]), which now motivates us to explore the time-frequency response of the structural motion.

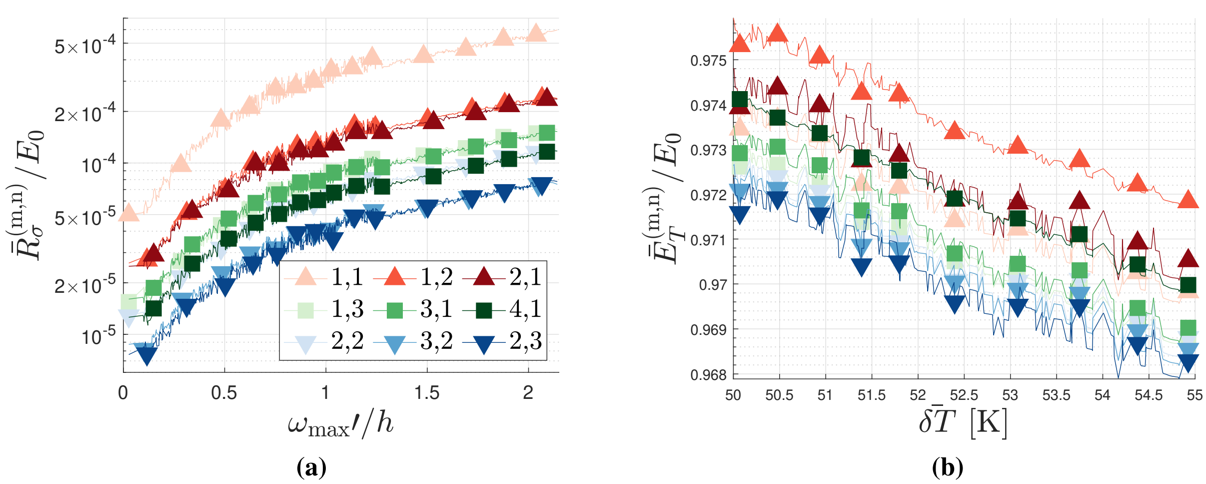

Fig. 16 (a) Normalized local mode stress plotted against the normalized quasi-static deflection, $\omega_{\max}'/h$ and (b) normalized local mode elastic modulus, $\bar{E}_T^{(\mathrm{m,n})}$, confined by the nodal lines of the selected modes against the panel-ramp temperature differential, $\bar{\delta T}$.

E. Temporal Evolution of Modal Characteristics

The SPOD analysis in Figure 12 depicts the average panel dynamics over the recorded test time. As Figures 14 and 16 make clear, however, the base panel state is changing with time, which can also be expected to lead to temporal

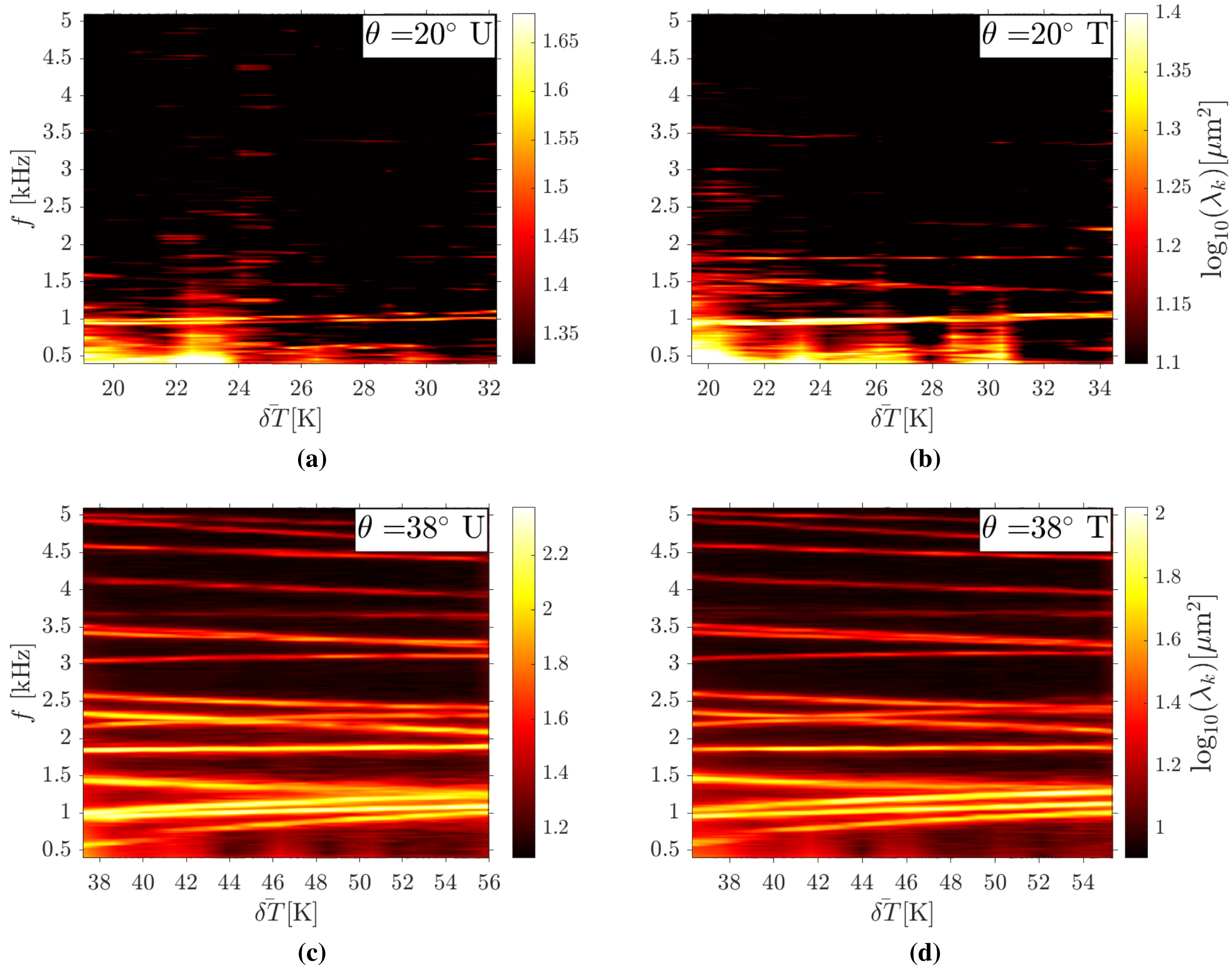

Fig. 17 Transient panel modal frequencies using short-time SPOD algorithm on the out-of-plane displacement measurements for (a,b) θ = 20°, and (c,d) θ = 38°, for untripped and tripped cases.

variations in the panel dynamics, in terms of both the vibratory frequency and power of each panel mode. To gain a better understanding of the temporal evolution of the frequencies of the various excited modes, we divide the out-of-plane panel motion data into 0.1 second segments with 50% overlap and compute the transient SPOD spectra as a function of the panel-ramp temperature differential, δT; examples are shown for the 20° and 38° ramps in Figure 17. Here we present data for a two-dimensional SWBLI with no flow trips (Figures 17a,c) and for the half-tripped SWBLI (Figures 17b,d). For both ramps, we see multi-directional frequency shifting with some modes tending to increase as $\delta\bar{T}$ grows, some tend to decrease in f, and some remain at a constant vibrational frequency. Beginning first with the 20° ramp, for both the untripped and half-tripped cases, we see evidence of the lower frequency modes - like (1,1), (1,2), and (2,1) - increasing in frequency with $\delta\bar{T}$; there are no discernible differences for the rate or overall magnitude of this increase between the two-dimensional and three-dimensional SWBLI. We do, however, see a very clear decrease in the (2,2) mode throughout the test time for the tripped flow case (Figure 17b) which is not readily apparent in the untripped case (Figure 17a); we also see minor evidence of the drop in frequency for the (3,2) mode in the tripped case that is not present in the untripped case. This suggests the asymmetric loading on the panel is indeed favoring the excitation and modification of modes with spanwise aligned antinodes. The 38° ramps in Figures 17c,d, in addition to showing significantly more activated modes, displays larger magnitude shifts in the vibrational frequencies. For both SWBLI cases we again see increases in the (1,1), (1,2), and (2,1) vibrational frequencies, and noticeable decreases in f for the (2,2), (2,3), and (3,2) modes. The mode shapes with fewer antinodes (i.e., the low-frequency modes) are seen to generally increase in vibrational frequency, meaning that the induced curvature and increased stress due to the static deflection shape dominate the transient behavior. Several other mode shapes, namely the (3,1) and (4,1) modes, however, show no evidence of frequency shifting as the panel heats and deforms, suggesting a balance between the static-deflection and thermal-softening effects, as suggested from Figure 16. The lack of significant differences in the transient behavior of the panel vibrations between the differing SWBLIs for the 38° ramp seem to indicate other factors besides the uniformity of $\delta\bar{T}$ are dictating panel dynamics.

To provide a more complete comparison of the evolving modal characteristics between the different ramp angles, we compute similar short-time SPOD spectra for each experiment and extract the frequency and vibrational power of selected modes throughout the test time. In Figure 18a, we present the time-varying modal frequencies for the first nine selected modes as functions of the panel-ramp temperature differential, δT, for all tests. The modes are grouped by color and marker type to indicate whether they increase in frequency (red triangles), decrease in frequency (blue nablas), or remain constant in frequency (green squares). In general, the lowest-frequency modes - (1,1), (1,2), and (2,1) - are more sensitive to panel curvature and internal stresses, whereas the (2,2), (2,3), and (3,2) modes appear to be more affected by thermal softening. There seems to be a balancing of these two effects for the (1,3), (3,1) and (4,1) modes, explaining the near-zero shifting in frequency observed. From Figure 16a we observed certain modes to lie in regions of elevated quasi-static stress compared to others. Thus in Figure 18b, these time-varying changes in frequency are now plotted against the modal stress factor, $\bar{R}_\sigma^{(\mathrm{m,n})}/E_0$. We see a clear trend emerge in that modes lying primarily in the relatively low regions of $\bar{R}_\sigma^{(\mathrm{m,n})}/E_0$ exhibit downward shifts in f, whereas the opposite is true for those in relatively high regions of $\bar{R}_\sigma^{(\mathrm{m,n})}/E_0$. The (1,3), (3,1) and (4,1) modes lie roughly in a middle range of $\bar{R}_\sigma^{(\mathrm{m,n})}/E_0$ (relative to the rest of the modes) and show negligible amounts of frequency shifting. There is some overlap in $\bar{R}_\sigma^{(\mathrm{m,n})}/E_0$ for differing directions of Δf's (especially near $\bar{R}_\sigma^{(\mathrm{m,n})}/E_0 \simeq 10^{-4}$); we look back to Figure 16b to provide a possible explanation for this. The (2,2) mode in this region displays a $\Delta f < 0$ and lies on a region of the panel where the thermal softening effect will be the greatest; the (1,2) and (2,1) modes both show increases in frequency and are on regions of the panel where the local curvature is largest and the thermal softening effects are reduced. We can also make comparisons to previous experiments on the same configuration at Mach 10 presented in ref. [10]. Although it is not readily obvious from the log scale, Figure 16a indicates an approximately linear relationship between $\bar{R}_\sigma^{(\mathrm{m,n})}/E_0$ and ω'_{max}/h. At Mach 10, normalized deflections up to $\omega'_{\mathrm{max}}/h \simeq 7$ where measured, from which we can infer that the modal stress factors were near an order-of-magnitude higher than in the present case,; this explains the tendency for mode frequencies to primarily increase throughout the recording time in ref. [10].

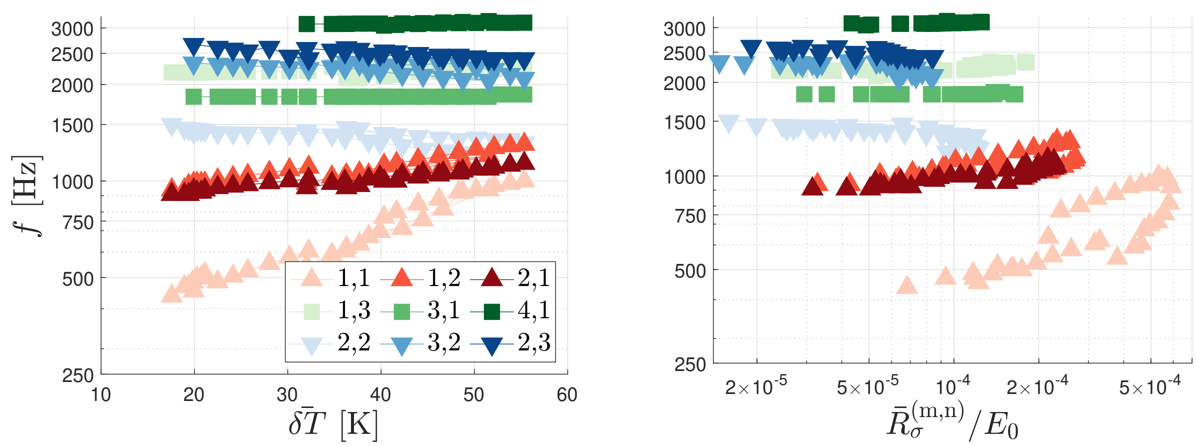

(a) **(b)**

Fig. 18 Time varying vibrational frequencies of selected modes for all ramp angles against (a) the panel-ramp temperature differential, δT, and (b) the modal internal stress factor.

In an attempt to collapse the data for the various modes, in Figure 19 we plot the normalized transient frequency of each mode (where f_0 is the wind-off frequency of the relevant mode) versus the modal stress factor. We see a noticeable convex relationship between f/f_0 and $\bar{R}_\sigma^{(\mathrm{m,n})}/E_0$, with a minimum loosely identified near $\bar{R}_\sigma^{(\mathrm{m,n})}/E_0 \simeq 10^{-4}$, though clearly additional factors (such as thermal softening) are present. Understanding the frequency shifting that occurs, we now examine the transient vibrational power contained within the specific mode shapes. In Figure 20a, we present the

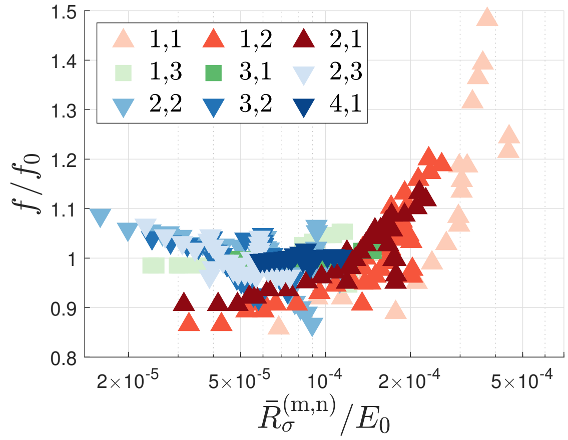

Fig. 19 Normalized time varying vibrational frequency of selected modes with respect to the modal internal stress factor.

initial modal powers for the various test conditions as well as for the $\theta = 38°$ ramp with no boundary-layer trips engaged. These mode-specific powers were computed by summing the eigenvalues within the full-width half-maximum of each peak in the short-time SPOD spectrum. These powers represent the 2σ mean of the vibratory amplitudes of the marker grid [27]. Representative of all the ramps examined, we note that as the vibrational frequency increases, the vibrational power of the selected mode generally decreases; this is generally consistent with the strengths of the peaks noted in the mean SPOD spectra in Figure 12. Clearly the (1,1), (1,2), and (2,1) modes, and to a lesser degree the (2,2) mode, represent a majority of panel vibrational motion. Comparing the untripped case of the 38° ramp to the tripped case, we see the dimensionality of the SWBLI doesn't affect the primary panel response (i.e., the same four modes contain a majority of the vibrational power). We do note that the spanwise aligned modes in the tripped case appear to show evidence of increases excitation compared to the untripped case, especially noticeable for the (2,2) mode near $f \simeq 1500$ Hz and the (3,2) mode near $f \simeq 2300$ Hz. Given the underlying base state of the panel is changing, we inspect for shifts in the modal power throughout the test time by examining the ΔP as a function of vibrational frequency in Figure 20b. Having shown in Figure 16 that the first three modes are severely affected by stiffening effects from growing quasi-static

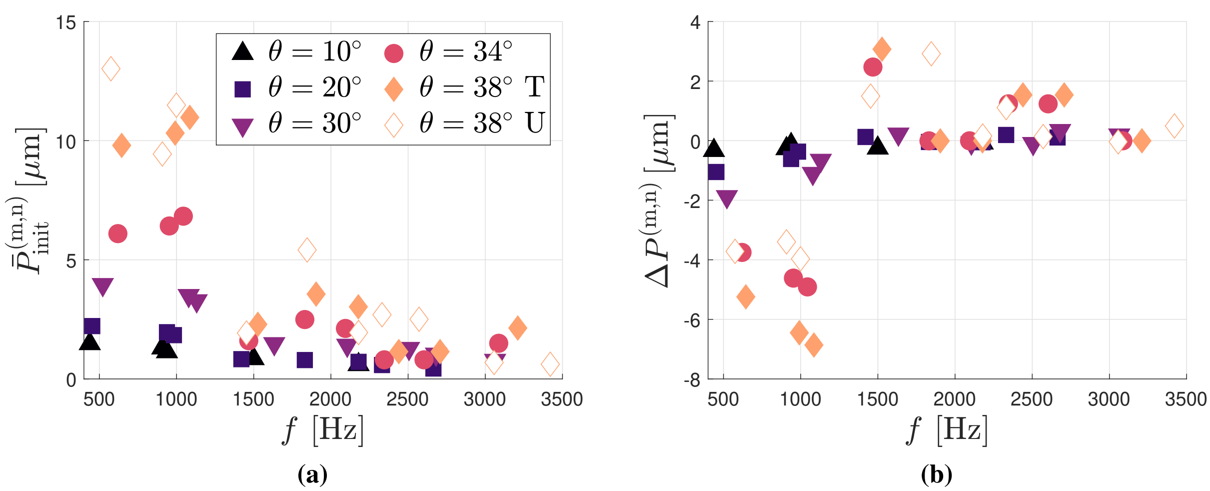

Fig. 20 (a) Initial modal power (solid markers represent half-tripped cases, open face markers represent the untripped case) and (b) shift in the modal power, both for the various ramp angles as functions of the initial vibrational frequency of each mode.

internal stresses, it follows that these modes shapes also experience a damping in their vibrational response. Conversely, we note the modes which experienced decreases in frequency as the panel heats (i.e., (2,2), (2,3), and (3,2)) showed an increase in vibrational power through the recording time; this is likely due to the reduction in stiffness experienced by these modes due to the thermal softening effects. Finally, those modes which displayed negligible frequency shifting (namely, (1,3), (3,1), and (4,1)) also displayed minimal changes in their vibrational power. We see the shifts in modal power is generally more pronounced for the half-tripped SWBLI case, which as we will see, experiences a larger change in quasi-static deflection throughout the test time.

The evolution of the total vibratory power of the panel for each ramp angle (and both the half-tripped and untripped cases) is examined in Figure 21 as a function of the maximum quasi-static deflection of the panel. To calculate this quantity, $\bar{A}$, we have summed the short-time SPOD eigenvalues between 300 Hz and 8000 Hz, subtracted the noise floor, normalized by the number of marker points, and taken the square root. As might be expected from our earlier results, $\bar{A}$ grows monotonically with ramp angle, suggesting that the overall increasing mechanical loading for the stronger SWBLI tends to dominate the bulk panel dynamics over any particular targeting of individual mode shapes through impingement. As we would expect from Figure 20a, the untripped SWBLIs on average produce slightly higher levels of $\bar{A}$. From Figure 20a we found the three lowest-frequency modes represent a majority of panel motion; given two of those modes ((1,1) and (2,1)) are streamwise aligned, this may indicate that the more span-uniform two-dimensional SWBLI gives more favorable loading conditions to excite these two modes, producing an elevated response as compared to the three-dimensional SWBLI. Similarly, from Figure 20b we would expect a general decrease in the average vibratory amplitude over time, and indeed this is what we see, indicating that deflection-induced stiffening dominates any thermal softening effects on the overall panel motion. In comparison to experiments at Mach 10 in ref. [10], here we find panel vibrations that are on average higher for similar ramp angles, likely due to the lesser quasi-static deflections at the present case, and thus lesser curvature induced stiffening to the panel.

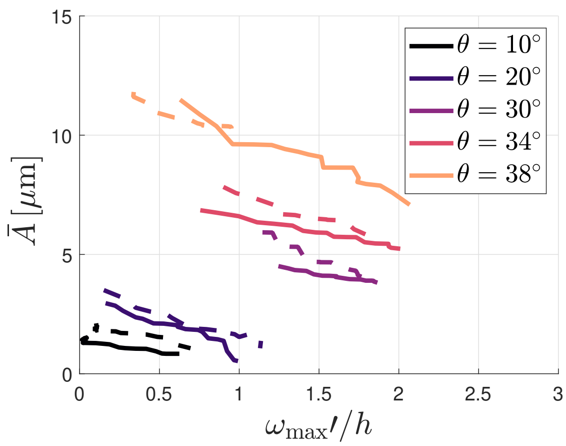

Fig. 21 Evolution of the average frequency-integrated vibratory amplitude derived from the SPOD eigenvalues (solid lines represent half-tripped case, dashed lines represent untripped case).

F. Modifications to Mode Shapes

Having characterized the temporal evolution of the modal vibrational characteristics, we end with a discussion of the mode shapes that exhibited spatial distributions deviating from clamped plate theory. In Figure 12c, the antinode location on the the non-tripped side of the plate lies where we would expect, whereas on the tripped side it is moved further upstream to be centered near $x/L \simeq 0.4$. Similar behavior was observed for all separated-flow cases, but it was most apparent for the $\theta = 38°$ case. A possible explanation for this is that, as the tripped side of the plate heats more quickly, the non-uniform thermal stress distribution influences the modal spatial distribution. To assess if this is true, we again employ the short-time SPOD algorithm to visualize the evolution of the (1,2) mode shape throughout the test time. Making use of the IR data, we can map these mode shapes to the temperature difference between the tripped and untripped sides, defined as $\delta T_{\text{span}} = T_{y/S=0.25} - T_{y/S=-0.25}$; we choose these values at the $x/L = 1/3$ streamwise location. Relevant results are plotted in Figure 22, with the maroon marker denoting the estimated antinode locations.

As the spanwise temperature gradient increases we clearly see that the tripped-side antinode moves further upstream, while the non-tripped side antinode remains stationary. One other possible explanation for this behavior, noting that the vibrational frequencies of the (1,2) and (2,1) modes are fairly close and increase at similar rates throughout the recorded test time, is an interaction between these two modes. In Figure 22f, we thus employ the analytical mode shapes for these two modes to derive the combined mode shape. This combined mode shape indeed shows significant movement of the antinode locations; however, upstream motion on one side is balanced by downstream motion on the other, which deviates from the experimental observations. We thus conclude that the movement of the tripped side antinode location is more likely due to the spanwise temperature gradient and note also that this shift is towards the area of the panel which experiences the highest temperatures, and thus the largest degree of thermal softening. We notice a somewhat similar phenomenon with the (2,2) mode, where again the antinode peaks on the tripped side of the plate are shifted slightly upstream, though the shifting was not as apparent as it is for the (1,2) mode. In all experiments, nothing of this nature occurred for modes with no spanwise antinodes (namely the (m,n=1) modes), indicating the asymmetric SWBLI aero-thermal loading was the influencing factor for this mode shape modification.

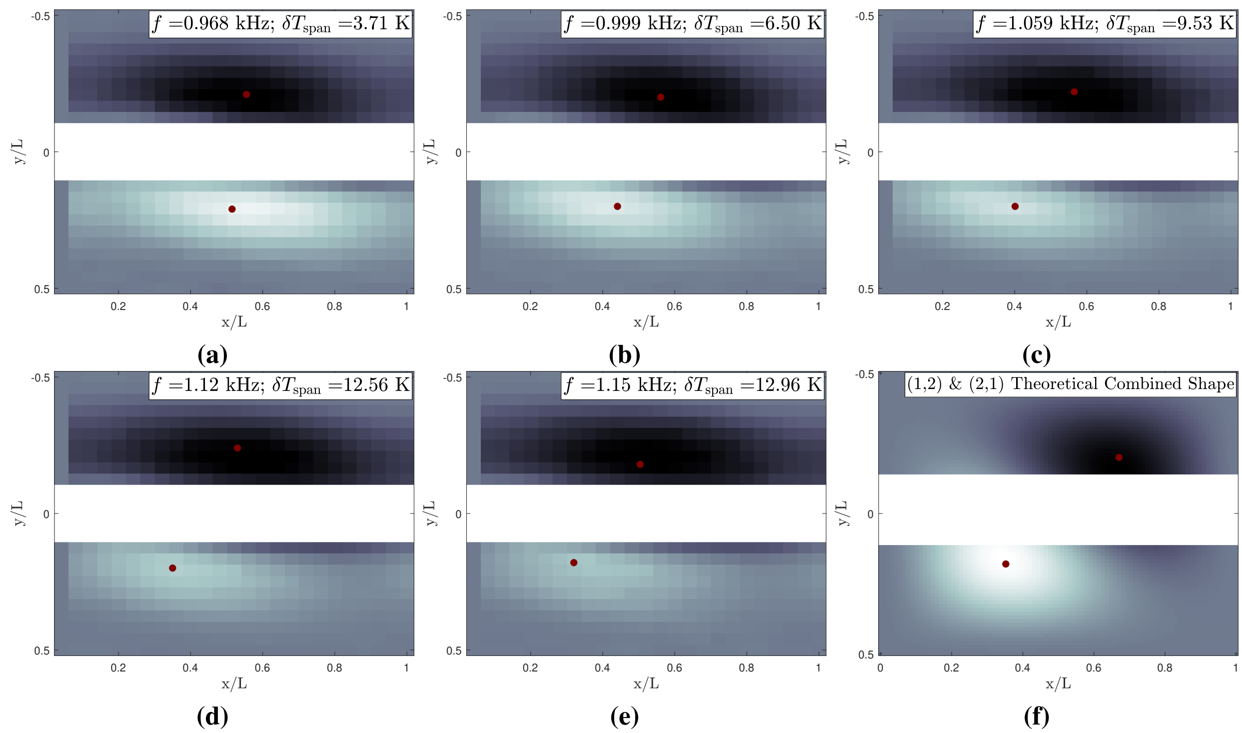

Fig. 22 (a-e) Evolution of the observed (1,2) mode shape as the spanwise temperature gradient, δT_{span}, increases in the $\theta = 38°$ experiments. (f) Theoretical combined mode shape between the (1,2) and (2,1) modes.

IV. Conclusions

There is a need to characterize the fluid-thermal-structural interactions that take place at hypersonic speeds in order to inform better design of reusable hypersonic vehicles. Given a real vehicle can potentially experience nonuniform boundary-layer transition, it is also of interest to characterize the FTSI for asymmetric aero-thermal loading conditions. In this work, the response of a clamped thin panel to a Mach-6, ramp-induced SWBLI has been experimentally characterized for a variety of ramp angles (10°, 20°, 30°, 34°, and 38°), under non-uniform streamwise and spanwise aero-thermal loads. Measurements of the underlying SWBLI flowfield using self-aligned focusing schlieren showed the SWBLI at the centerline to vary from attached at 10° to fully separated for $\theta \geq 30°$. IR thermography detailed the spatial-temporal thermal loading across the compliant panel and the clamped boundaries, providing insight into the degree of thermal strain introduced for each ramp angle and flow condition. Fast-response pressure transducers showed the spectra of the fluid loading and found that for all ramp angles and both flow conditions, elevated unsteadiness was observed in the frequency range of the compliant panel natural structural modes. The presence of the boundary-layer trips was found to produce a spanwise non-uniformity in the mechanical and thermal loading, which resulted in higher levels of pressure unsteadiness and heating on the tripped half of the plate. For some compression angles, this resulted in spanwise temperature differentials as high as 20 K.

When combined with a Spectral Proper Orthogonal Decomposition analysis, the applied high-accuracy photogrammetry technique allowed both the frequencies and out-of-plane displacement distributions of the dominant panel modes to be uncovered under the various conditions. For all cases the regular (m,n) mode shapes from classical plate theory were present and dominated panel motion, though they were found to lie at somewhat higher frequencies than determined through pre-tunnel modal testing, likely due to the growing static deflections experienced throughout each test. Further, select modes experienced spatial modifications to their mode shapes, likely due to the spanwise temperature gradients on the panel. Noticeable shifts in frequency were observed during the recorded test time, indicating that the already complex fluid-structural interaction induced by the SWBLI becomes more involved when considering the heating-induced transient shifts in the modal vibrational frequencies. The spatial-temporal surface stresses were computed and used to provide a proxy for the level of stiffening present in each mode. It was found that modes containing the highest normalized internal stresses tended to increase in vibrational frequency and decrease in vibrational power, whereas modes with the lowest stresses exhibited opposite behavior. These noticeable changes to the vibrational characteristics have meaningful implications for both potential flow feedback as well as long-term panel fatigue considerations. These stresses were tied to static deformations, likely caused by compressive thermal and normal strains, and affected primarily lower-frequency modes. The downward frequency shifting, more prevalent among higher-frequency modes, appeared instead to be linked to thermal softening from panel heating. Comparisons were made between the present half-tripped SWBLI cases and experiments on the same model with an untripped flow. We generally found the half-tripped case to preferentially favor excitation of spanwise aligned mode shapes (such as the (2,2) mode), though the three-dimensional SWBLI produced a lesser overall vibrational response.

References

[1] McNamara, J., and Friedmann, P., "Aeroelastic and Aerothermoelastic Analysis in Hypersonic Flow: Past, Present, and Future," *AIAA Journal*, Vol. 49, 2011. https://doi.org/10.2514/1.J050882.

[2] Eason, T., and Spottswood, S., "A Structures Perspective on the Challenges Associated with Analyzing a Reusable Hypersonic Platform," *54th AIAA/ASME/ASCE/AHS/ASC Structures, Structural Dynamics, and Materials Conference*, 2013. https://doi.org/10.2514/6.2013-1747.

[3] Zuchowski, B., "Predictive Capability for Hypersonic Structural Response and Lift Prediction, Phase I - Identification of Knowledge Gaps," Tech. rep., Air Force Research Laboratory, 2010.

[4] Zuchowski, B., "Predictive Capability for Hypersonic Structural Response and Lift Prediction, Phase II - Detailed Design of Hypersonic Cruise Vehicle Hot-Structure," Tech. rep., Air Force Research Laboratory, 2012.

[5] Spottswood, S. M., Eason, T., and Beberniss, T., "Full-Field, Dynamic Pressure and Displacement Measurements of a Panel Excited by Shock Boundary-Layer Interaction," *19th AIAA/CEAS Aeroacoustics Conference*, 2013. https://doi.org/10.2514/6.2013-2016.

[6] Clemens, N. T., and Narayanaswamy, V., "Low-Frequency Unsteadiness of Shock Wave/Turbulent Boundary Layer Interactions," *Annual Review of Fluid Mechanics*, Vol. 46, No. Volume 46, 2014, 2014, pp. 469–492. https://doi.org/https://doi.org/10.1146/annurev-fluid-010313-141346.

[7] Whalen, T., Kennedy, R., Laurence, S., Sullivan, B., Bodony, D., and Buck, G., "Unsteady Surface and Flowfield Measurements in Ramp-Induced Turbulent and Transitional Shock-Wave Boundary-Layer Interactions at Mach 6," *AIAA Scitech 2019 Forum*, 2019. https://doi.org/10.2514/6.2019-1127.

[8] Eitner, M., Yoo-Jin, A., Jayant, S., and Clemens, N., "Measurements of Clamped Panel Vibration Under a Ramp-Induced Shock/Bundary Layer Interaction with Constrained Layer Damping," *Journal of Fluids and Structures*, Vol. 136, 2025, p. 104333. https://doi.org/https://doi.org/10.1016/j.jfluidstructs.2025.104333.

[9] Kronheimer, M. J., Thayer, J. D., McNamara, J. J., and Gaitonde, D. V., "Assessment of Aeroelastic Coupling Between a Shock Boundary Layer Interaction and a Flexible Panel," *Journal of Fluids and Structures*, Vol. 133, 2025, p. 104271. https://doi.org/https://doi.org/10.1016/j.jfluidstructs.2025.104271.

[10] Duchene, T., Schöneich, A., Bathel, B., Weisberger, J., Buck, G., Bodony, D., and Laurence, S., "Experimental Study of Fluid-Thermal-Structural Interactions in a Mach-10 Compression Corner Using Super-Ellipse-Based Photogrammetry." *Experiments in Fluids*, Vol. 67, No. 53, 2026. https://doi.org/https://doi.org/10.1007/s00348-026-04209-y.

[11] Dowell, E., "Nonlinear Oscillations of a Fluttering Plate," *AIAA Journal*, Vol. 4, No. 7, 1966, pp. 1267–1275. https://doi.org/10.2514/3.3658.

[12] Gee, D., and Sipic, S., "Coupled Thermal Model for Nonlinear Panel Flutter," *AIAA Journal*, Vol. 37, No. 5, 1999, pp. 642–650. https://doi.org/10.2514/2.765.

[13] Librescu, L., Marzocca, P., and Silva, W., "Linear/Nonlinear Supersonic Panel Flutter in a High-Temperature Field," *Journal of Aircraft*, Vol. 41, 2004, pp. 918–924. https://doi.org/10.2514/1.679.

[14] LaFontaine, J., Gogulapati, A., and McNamara, J., "Effects of Strain Hardening on Response of Skin Panels in Hypersonic Flow," *AIAA Journal*, Vol. 54, No. 6, 2016, pp. 1974–1986. https://doi.org/10.2514/1.J054582.

[15] Budiansky, B., and Mayers, J., "Influence of Aerodynamic Heating on the Effective Torsional Stiffness of Thin Wings," *Journal of the Aeronautical Sciences*, Vol. 23, No. 12, 1956, pp. 1081–1093. https://doi.org/10.2514/8.3735.

[16] Gupta, K., Choi, S., Lung, S., and Ibrahim, A., "Aerothermoelastic-Acoutics Simulation of Flight Vehicles," *AIAA Journal*, Vol. 55, No. 1, 2017, pp. 49–56. https://doi.org/10.2514/1.J055088.

[17] Heeg, J., Gilbert, M., and Pototzky, A., "Active Control of Aerothermoelastic Effects for a Conceptual Hypersonic Aircraft," *Journal of Aircraft*, Vol. 30, No. 4, 1993, pp. 453–458. https://doi.org/10.2514/3.56890.

[18] Heeg, J., Gilbert, M., and Pototzky, A., "Aerothermoelastic Analysis of a NASP Demonstrator Model," Tech. rep., NASA, 1993.

[19] Pham, H. T., Gianikos, Z. N., and Narayanaswamy, V., "Compression Ramp Induced Shock-Wave/Turbulent Boundary-Layer Interactions on a Compliant Material," *AIAA Journal*, Vol. 56, No. 7, 2018, pp. 2925–2929. https://doi.org/10.2514/1.J056652.

[20] Eitner, M. A., Ahn, Y.-J., Musta, M. N., Sirohi, J., and Clemens, N., "Effect of Ramp-Induced Shock/Boundary Layer Interaction on the Vibration of A Compliant Panel at Mach 5," *AIAA Scitech 2023 Forum*, 2022. https://doi.org/10.2514/6.2023-0081.

[21] Ahn, Y.-J., Sirohi, J., and Clemens, N. T., "Experimental Study of the Fluid-Structure Interaction Induced by a Mach 5 Compression Ramp-SBLI," *AIAA Scitech 2025 Forum*, 2025. https://doi.org/10.2514/6.2025-1308.

[22] Riley, Z. B., and McNamara, J. J., "Interaction Between Compliant Structures and Boundary-Layer Transition in Hypersonic Flow," *AIAA Journal*, Vol. 55, No. 8, 2017, pp. 2645–2663. https://doi.org/10.2514/1.J055521.

[23] Brouwer, K. R., Perez, R. A., Riley, Z. B., Beberniss, T. J., and Spottswood, S. M., "Measurements of a Thermally Buckled Panel Dynamically Excited by a Separated Shock/Boundary-Layer Interaction," *Aerospace Science and Technology*, Vol. 168, 2026, p. 111066. https://doi.org/https://doi.org/10.1016/j.ast.2025.111066.

[24] Dolling, D. S., "Fifty Years of Shock-Wave/Boundary-Layer Interaction Research: What Next?" *AIAA Journal*, Vol. 39, No. 8, 2001, pp. 1517–1531. https://doi.org/10.2514/2.1476.

[25] Ganapathisubramani, B., Clemens, N. T., and Dolling, D. S., "Effects of Upstream Boundary Layer on the Unsteadiness of Shock-Induced Separation," *Journal of Fluid Mechanics*, Vol. 585, 2007, p. 369–394. https://doi.org/10.1017/S0022112007006799.

[26] Gaitonde, D., "Progress in Shock Wave/Boundary Layer Interactions," *Progress in Aerospace Sciences*, Vol. 72, 2015, pp. 80–99. https://doi.org/https://doi.org/10.1016/j.paerosci.2014.09.002.

[27] Whalen, T., Schoneich, A., Laurence, S., Sullivan, B., Bodony, D., Freydin, M., Dowell, E., and Buck, G., "Hypersonic Fluid–Structure Interactions in Compression Corner Shock-Wave/Boundary-Layer Interaction," *AIAA Journal*, Vol. 58, No. 9, 2020, pp. 4090–4105. https://doi.org/10.2514/1.J059152.

[28] Schöneich, A. G., Laurence, S. J., Dettenrieder, F., Bodony, D., Buck, G., Weisberger, J., and Bathel, B., "Hypersonic Fluid-Thermal-Structural Interactions on a Compression Ramp with an Embedded Compliant Panel," *AIAA AVIATION 2023 Forum*, 2023. https://doi.org/10.2514/6.2023-3851.

[29] Berger, K. T., Hollingsworth, K. E., Wright, S. A., and Rufer, S. J., "NASA Langley Aerothermodynamics Laboratory: hypersonic testing capabilities," *53rd AIAA aerospace sciences meeting*, 2015, p. 1337.

[30] Hurst, A. M., Olsen, T. R., Goodman, S., VanDeWeert, J., and Shang, T., *An Experimental Frequency Response Characterization of MEMS Piezoresistive Pressure Transducers*, 2014, Vol. Volume 6: Ceramics; Controls, Diagnostics and Instrumentation; Education; Manufacturing Materials and Metallurgy. https://doi.org/10.1115/GT2014-27159.

[31] Freydin, M., and Dowell, E. H., "Fully Coupled Nonlinear Aerothermoelastic Computational Model of a Plate in Hypersonic Flow," *AIAA Journal*, Vol. 59, No. 7, 2021, pp. 2725–2736. https://doi.org/10.2514/1.J060085.

[32] Bathel, B. F., and Weisberger, J. M., "Compact, Self-Aligned Focusing Schlieren System," *Optical Letter*, Vol. 15, No. 46, 2021, pp. 3328–3331. https://doi.org/10.1364/OL.428011.

[33] Bathel, B. F., and Weisberger, J. M., "Development of a Self-Aligned Compact Focusing Schlieren System for NASA Test Facilities," *AIAA Scitech 2022 Forum*, 2022. https://doi.org/10.2514/6.2022-0560.

[34] Bathel, B. F., Weisberger, J. M., Page, W. E., Lalonde, E. J., and Jones, S. B., "Digital Self-Aligned Focusing Schlieren," *Opt. Lett.*, Vol. 49, No. 4, 2024, pp. 778–781. https://doi.org/10.1364/OL.511274.

[35] Walker, S., Thomas, A., and Taylor, G., "Photogrammetric Reconstruction of High-Resolution Surface Topographies and Deformable Wing Kinematics of Tethered Locusts and Free-Flying Hoverflies," *Journal of The Royal Society Interface*, Vol. 6, No. 33, 2009, pp. 351–366. https://doi.org/10.1098/rsif.2008.0245.

[36] Schöneich, A. G., Whalen, T. J., Laurence, S. J., Sullivan, B. T., Bodony, D. J., Freydin, M., Dowell, E. H., Stacey, L. J., and Buck, G. M., "Fluid-Thermal-Structural Interactions in Ramp-Induced Shock-Wave Boundary-Layer Interactions at Mach 6," *AIAA Scitech 2021 Forum*, 2021. https://doi.org/10.2514/6.2021-0912.

[37] Fischer, M. C., "Spreading of a Turbulent Disturbance," *AIAA Journal*, Vol. 10, No. 7, 1972, pp. 957–959. https://doi.org/10.2514/3.50265.

[38] Towne, A., Schmidt, O. T., and Colonius, T., "Spectral Proper Orthogonal Decomposition and its Relationship to Dynamic Mode Decomposition and Resolvent Analysis," *Journal of Fluid Mechanics*, Vol. 847, 2018, p. 821–867. https://doi.org/10.1017/jfm.2018.283.

[39] Kegerise, M., and Rufer, S., "Unsteady Heat-Flux Measurements of Second-Mode Instability Waves in a Hypersonic Flat-Plate Boundary Layer," *Experiments in Fluids*, 2016. https://doi.org/10.1007/s00348-016-2214-9.

[40] Coleman, G. T., and Stollery, J. L., "Heat Transfer from Hypersonic Turbulent Flow at a Wedge Compression Corner," *Journal of Fluid Mechanics*, Vol. 56, No. 4, 1972, p. 741–752. https://doi.org/10.1017/S0022112072002630.

[41] Young, D. H., "Vibration of Rectangular Plates by the Ritz Method," *Journal of Applied Mechanics-transactions of The Asme*, Vol. 17, 1950. URL https://api.semanticscholar.org/CorpusID:114094870.

[42] Levy, S., "Bending of rectangular plates with large deflections," Tech. rep., US Government Printing Office, 1942.

[43] Pinho, F. A. X. C., Amabili, M., Prado, Z. J. G. N. D., and da Silva, F. M. A., "Nonlinear Free Vibration Analysis of Doubly Curved Shells," *Nonlinear Dynamics*, , No. 111, 2023, pp. 21535–21555. https://doi.org/doi.org/10.1007/s11071-023-08963-0.